Article

Current Biology

ERK-mediated curvature feedback regulates branching morphogenesis in lung epithelial tissue

Graphical abstract

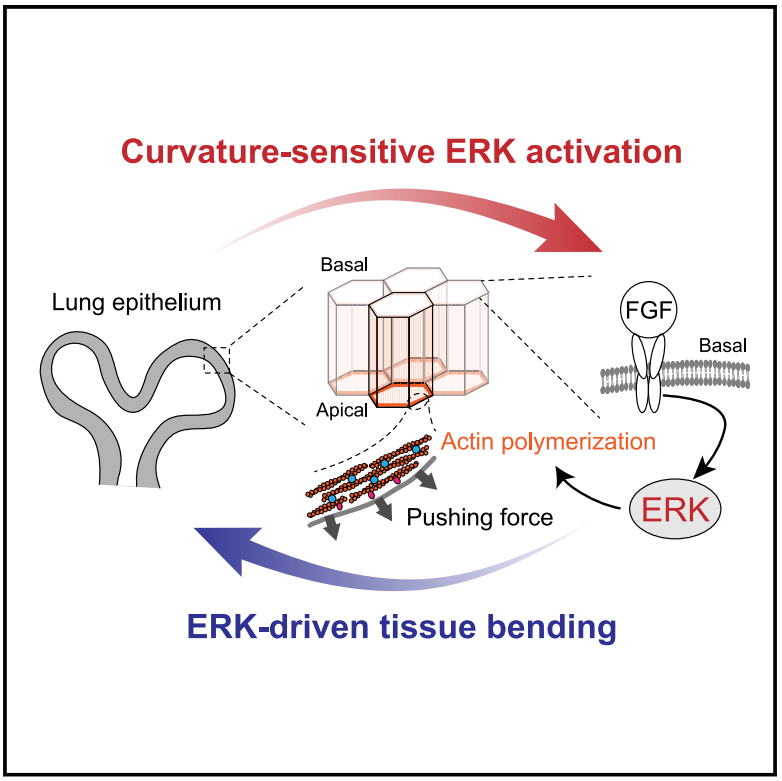

Authors

Tsuyoshi Hirashima,
Michiyuki Matsuda

Correspondence

thira@nus.edu.sg

In brief

Tissue curvature influences and arises from cellular behaviors, yet the mechanism for tissue morphogenesis remains unclear. By employing developing lungs, Hirashima et al. demonstrate that ERK mediates curvature sensing and force generation in epithelial cells, forming a negative feedback loop that leads to repetitive branching patterning.

Highlights

- ERK activity aligns with curvature of epithelial sheet in developing murine lungs
- Tissue curvature regulates ERK activity through endocytosis of extracellular FGF1
- ERK activation promotes actin polymerization, reducing tissue curvature
- Negative feedback links ERK activity and tissue curvature in iterative branching

Hirashima & Matsuda, 2024, Current Biology *34*, 683–696
February 26, 2024
https://doi.org/10.1016/j.cub.2023.12.049

CellPress

Current Biology

CellPress
OPEN ACCESS

Article

ERK-mediated curvature feedback regulates branching morphogenesis in lung epithelial tissue

Tsuyoshi Hirashima[1,2,3,4,5,8,9,*] and Michiyuki Matsuda[4,6,7]

[1]Mechanobiology Institute, National University of Singapore, 5A Engineering Drive 1, Singapore 117411, Singapore
[2]Department of Physiology, Yong Loo Lin School of Medicine, National University of Singapore, 2 Medical Drive MD9, Singapore 117593, Singapore
[3]The Hakubi Center, Kyoto University, Yoshida-honmachi, Kyoto 606-8501, Japan
[4]Graduate School of Biostudies, Kyoto University, Yoshidakone-cho, Kyoto 606-8501, Japan
[5]Japan Science and Technology Agency, PRESTO, 4-1-8 Honchō, Kawaguchi 332-0012, Japan
[6]Graduate School of Medicine, Kyoto University, Yoshidakone-cho, Kyoto 606-8501, Japan
[7]Institute for Integrated Cell-Material Sciences, Kyoto University, Yoshida-honmachi, Kyoto 606-8317, Japan
[8]X (formerly Twitter): @hirashima0203
[9]Lead contact
*Correspondence: thira@nus.edu.sg
https://doi.org/10.1016/j.cub.2023.12.049

SUMMARY

Intricate branching patterns emerge in internal organs due to the recurrent occurrence of simple deformations in epithelial tissues. During murine lung development, epithelial cells in distal tips of the single tube require fibroblast growth factor (FGF) signals emanating from their surrounding mesenchyme to form repetitive tip bifurcations. However, it remains unknown how the cells employ FGF signaling to convert their behaviors to achieve the recursive branching processes. Here, we show a mechano-chemical regulatory system underlying lung branching morphogenesis, orchestrated by extracellular signal-regulated kinase (ERK) as a downstream driver of FGF signaling. We found that tissue-scale curvature regulated ERK activity in the lung epithelium using two-photon live cell imaging and mechanical perturbations. ERK activation occurs specifically in epithelial tissues exhibiting positive curvature, regardless of whether the change in curvature was attributable to morphogenesis or perturbations. Moreover, ERK activation accelerates actin polymerization preferentially at the apical side of cells, mechanically contributing to the extension of the apical membrane, culminating in a reduction of epithelial tissue curvature. These results indicate the existence of a negative feedback loop between tissue curvature and ERK activity that transcends spatial scales. Our mathematical model confirms that this regulatory mechanism is sufficient to generate the recursive branching processes. Taken together, we propose that ERK orchestrates a curvature feedback loop pivotal to the self-organized patterning of tissues.

INTRODUCTION

Characteristic patterns are generated in developing tubular organs through the repeated occurrence of tissue morphogenetic modes, such as elongation, bending, and bifurcation.[1–3] During murine lung development, the complex branched architecture is stereotypically created from a simple epithelial tube, by assembling morphogenetic modes as building motifs with a spatiotemporal order.[2] Genetic investigations conducted earlier have unveiled pivotal molecules and signaling pathways underlying lung epithelial morphogenesis.[4–6] Moreover, previous studies have proposed how cellular behaviors and mechanical forces determine the tube shape.[7–9] Thus, the interplay between chemical signals and cell mechanics in constituent cells determines the organized periodic branched pattern, although it is not completely understood yet.

Several pharmacological and genetic studies have demonstrated that fibroblast growth factor (FGF) signaling is a key regulator of lung branching morphogenesis during murine development.[10] Treating an isolated epithelium, from which the mesenchyme has been excised, with various FGF ligands has elucidated the distinct roles of FGFs in shaping lung epithelial morphology. For example, FGF1 and FGF10 induce bud formation, whereas FGF7 gives rise to a balloon-like shape, and any of these ligands could promote epithelial proliferation.[11–13] An investigation of the spatiotemporal expression pattern uncovered the fact that *Fgf10* is expressed locally in the mesenchyme surrounding the distal bud of the lung epithelium,[13] and its main receptor, *Fgfr2b*, is homogeneously expressed in the lung epithelium.[11] These results led to hypothesize that the *Fgf10* prepattern initiates branching during lung development[13]; this was partially supported by results of previous studies on mice in which *Fgf10* or its main receptor *Fgfr2b* were knocked out and showed the complete absence of lungs.[14–16] However, it was demonstrated that the ubiquitous overexpression of *Fgf10* in its knocked out background could restore the branching

process,[17] indicating that the *Fgf10* expression is required, but the precise prepattern is dispensable for the murine lung branching morphogenesis. Thus, we explored how FGF signals are converted to cellular behaviors underlying tissue morphogenesis.

A main FGF downstream signaling pathway, the extracellular signal-regulated kinase (ERK)/MAP kinase pathway, includes a three-tiered kinase cascade, i.e., RAF-MEK-ERK.[10] The genetic inactivation of either *Mek1/2* or Erk1/2 specifically in the airway epithelium results in lung agenesis,[18] implying that ERK and its activation were essential for lung development.[19] Previously, immunofluorescence staining results suggested that the phosphorylation of ERK was most likely to occur in the distal tips of the lung epithelium and may, thus, be involved in the budding process during lung development.[20–22] FGFR2-mediated ERK activation reportedly upregulates the expression of *Anxa4*, whose products are able to bind with F-actin bundles, and promotes cell migration within epithelial tissues.[20] These reports revealed the role of ERK activity in cellular behavior during lung development. However, it is still unclear how the epithelial cells collectively behave to generate the periodic branching morphogenesis mediated via ERK signaling.

In this study, we show a mechano-chemical basis for self-sustained branching morphogenesis by combining two-photon live cell imaging of a Förster resonance energy transfer (FRET)-based biosensor, mechanical perturbation, and mathematical modeling. We find that ERK activation occurs specifically in epithelial tissues with a positive curvature and promotes cell extension through actin polymerization at the apical edges, resulting in a decreased tissue curvature. Thus, our study clarifies that the negative feedback loop between the tissue curvature and ERK activity underlies the process of repetitive branching morphogenesis in developing murine lung epithelial tissues.

RESULTS

ERK activity is correlative to tissue curvature of lung epithelium

We first examined the impact of ERK activity on lung epithelial morphology during murine development. We cultured developing murine lungs dissected at embryonic day (E) 12.5 in the presence or absence of PD0325901, an inhibitor of the ERK activator MEK, under explant culture conditions. Treatment with the MEK inhibitor significantly impeded the growth of lung epithelial tissues cultured for 1 day (Figures 1A and 1B), aligning with findings from prior genetic studies.[18,22] This indicates the importance of ERK activation for epithelial morphogenesis during this stage.

Then, we visualized the spatial distribution of ERK activity in lung lobes dissected from murine embryos that ubiquitously expressed the cytoplasmic FRET biosensor for the ERK activity[23–25] via whole-tissue two-photon live imaging (Figure 1C; Video S1A). FRET images showed that the ERK activity in the epithelium was well correlated with tissue curvature; the ERK activity was higher in the curved sheet protruding the mesenchyme (convex), whereas it was lower in the sheet bent toward the lumen (concave) (Figure 1C). Although endothelial cells exhibited relatively high levels of ERK activity, they were less involved in epithelial branching morphogenesis[26]; thus, we focused on ERK activity in the epithelial tissues. The basal surface of the epithelial tissues was extracted for quantification, and positions at nodes of generated meshes were embedded on the surface, enabling us to map chemical and geometrical quantities, such as ERK activity, epithelial tissue curvature, and tissue thickness (Figures 1D and S1A). As expected, there is a positive correlation between the ERK activity and tissue curvature ($\rho = 0.51$, where ρ is the Spearman's rank correlation coefficient; Figures 1E, 1G, and S1B), which indicates that ERK activation would occur mainly in convex regions. The curvature-dependent ERK activation was observed in the developing lung epithelium under the explant culture condition (Figure 1H; Video S1B). Moreover, there is a negative correlation between the ERK activity and tissue thickness ($\rho = -0.48$; Figures 1F and 1G). As observed in distal buds, the epithelial tissue was thinner in the tip region, where ERK was activated, than in the stalk region, where ERK was inactivated (Figure 1I). These results suggest the existence of interplay between the ERK activity and cell morphology in developing murine lungs.

ERK activity follows morphological change of isolated epithelial tissues

To analyze how ERK activity is regulated in the lung epithelium, we isolated epithelial tissues from mesenchymal tissues and embedded them in Matrigel with culture media containing FGFs for *ex vivo* culture (Figure 2A). This simplified experimental system allows us to explore epithelial response to external chemical and mechanical stimuli under regulated conditions. As reported previously,[11,12] treatment with 500 ng mL^{-1} FGF1 for 1 day induced branched epithelial buds, whereas treatment with 100 ng mL^{-1} FGF7 gave rise to a cyst-like structure with an enlarged lumen (Figure 2B). PD0325901 treatment with FGF1 resulted in the collapse of the lumen and absence of large deformations; this was also observed with the absence of growth factors with 1-day-old culture (Figure 2B). We then examined the spatial distribution of ERK activity in epithelial tissues, 1 h after chemical treatment, prior to the initiation of any tissue morphological changes. FGF1 activated ERK exclusively at the distal buds in a manner similar to that observed with the mesenchyme (Figure 1C), through ligand endocytosis from the basal side of cells (Figures S2A–S2C; Video S2), despite the homogeneous expression of four FGF receptors, i.e., FGFR1, FGFR2, FGFR3, and FGFR4 in the distal epithelial tissues.[11,17,27,28] In contrast, FGF7 activated the ERK almost homogeneously in the epithelial tissues (Figure 2C). This homogeneous ERK activation was maintained during the tissue morphogenetic process (Figure S2D; Video S3A). As expected, ERK activity was homogeneously low in epithelial cells treated with PD0325901 or cultured without any growth factors (Figure 2C). These results suggest that localized ERK activation at the distal tips is key to the process of branching morphogenesis.

To examine the spatiotemporal dynamics of ERK activity during the branching of isolated epithelial tissues, we performed two-photon live imaging under FGF1 supplemented conditions. We found that the ERK activity increased during the protrusion of epithelial tips and decreased when the tip apex became flat during the tip bifurcation process (Figure 2D; Video S3B). Notably, no mesenchymal cells were observed around the distal tip of the epithelium (Figure 2D; Video S3B), suggesting that tip

CellPress
OPEN ACCESS

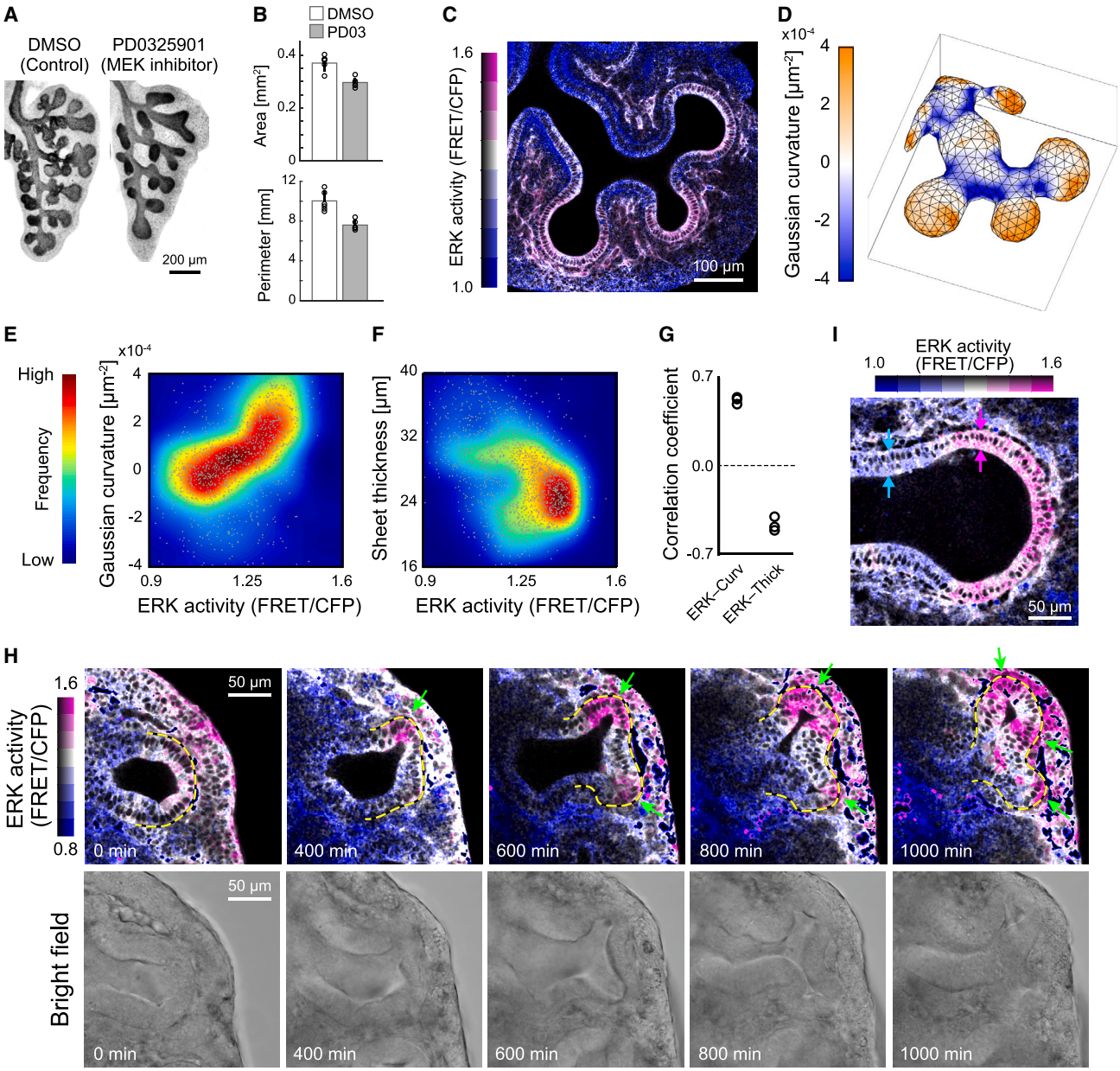

Figure 1. Relationship between ERK activity and tissue geometry in epithelium of intact lung lobes

(A) Immunofluorescence images of anti-E-cadherin staining in an explant culture of the murine lungs for 1 day dissected from E12.5, after treatment with dimethyl sulfoxide (DMSO) as a control (left) and 1 μM PD0325901 as a specific MEK inhibitor (right). Scale bars, 200 μm.

(B) Area and perimeter of epithelial tissues from the projected images. The number of buds: 34.2 ± 2.8 for the DMSO control and 19.2 ± 2.8 for the PD0325901 treatment. Data represent mean and SD values. N = 5, two-sample t test, $p < 0.001$.

(C) Representative ERK activity map in a developing lung at E12.5. Scale bars, 100 μm.

(D) Gaussian curvature map on the basal side of the lung epithelium.

(E and F) Scatterplot of ERK activity versus Gaussian curvature (E) and that of ERK activity versus sheet thickness (F). Color indicates frequency. n = 1,495 for (E) and 1,743 for (F), N = 3.

(G) Correlation coefficient of (E) and (F). N = 3, one-sample t test, $p = 0.001$ (E) and $p = 0.004$ (F).

(H) Time-lapse images of ERK activity (upper) and bright field (lower) during terminal bifurcation of an epithelium in the intact lung lobe under the explant culture condition. Yellow dotted line represents the basal side of the epithelial tissue. Green arrows represent the ERK activation. Scale bars, 50 μm.

(I) ERK activity map in the distal region of a lung dissected at E12.5. Arrows facing each other indicate the sheet thickness at the distal tip (magenta) and the distal stalk (blue). Scale bars, 50 μm.

See also Figure S1, Video S1, and Data S1.

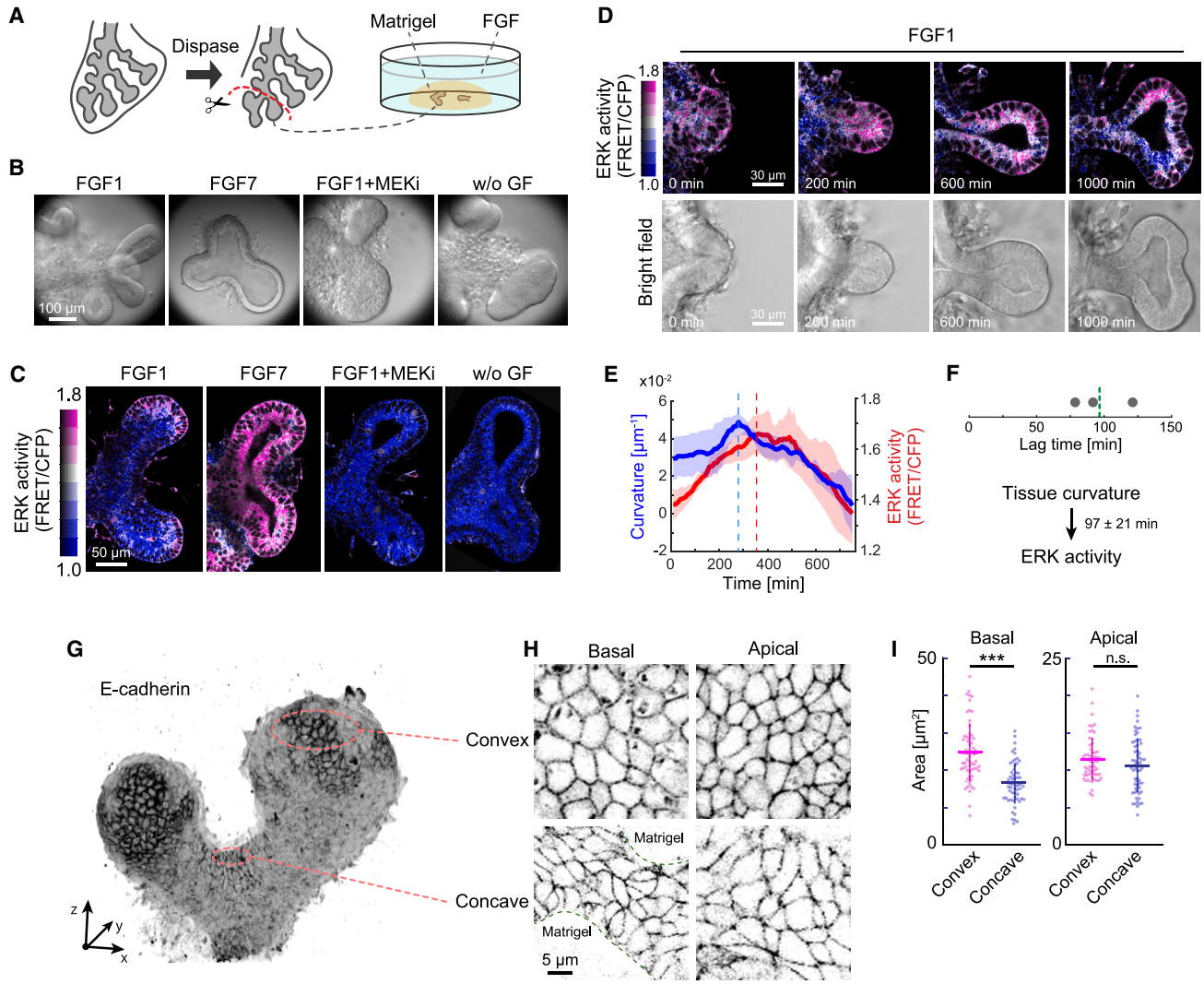

Figure 2. ERK activity and tissue curvature in the isolated epithelium

(A) Schematics of the culture system for the isolated lung epithelial tissues.

(B) Bright-field images of isolated epithelial tissues subjected chemical treatments for 1 day from E12.5. Concentrations: 500 ng mL^{-1} FGF1, 100 ng mL^{-1} FGF7, 1 μM PD0325901 (MEKi). Scale bars, 100 μm.

(C) ERK activity of isolated epithelial tissues subjected to chemical treatments shown in (B) for 1 h from E12.5. The administration duration was considerably brief when juxtaposed with the time scale of tissue morphogenesis. Consequently, the epithelial tissues maintained a consistent shape in all cases, while exhibiting distinct ERK activity patterns. Scale bars, 50 μm.

(D) Time-lapse images of ERK activity (upper) and bright field (lower) in the case of 500 ng mL^{-1} FGF1 treatment to the isolated lung epithelial tissue. Time origin is at 4 h after the FGF1 treatment. Scale bars, 30 μm.

(E) Tissue curvature (blue) and ERK activity (red) at the tip apex over time. The time courses of each sample were aligned with respect to the peak point of tissue curvature. Vertical dotted lines indicate the peak time for the tissue curvature and ERK activity, respectively. Data represent mean and SD values. N = 3.

(F) Lag time from the peak for tissue curvature to the peak for ERK activity. N = 3.

(G and H) The whole-mount immunofluorescence of anti-E-cadherin for FGF1-treated isolated lung epithelial tissues. Three-dimensional rendering image (G), and sectional images of basal and apical sides in each convex and concave region. Scale bars, 5 μm.

(I) Basal area (left) and apical area (right) of individual cells in the convex and concave regions of isolated epithelial tissues. Bold and error bars represent the mean and SD values, respectively. n = 60, N = 3. Welch's t test, $p < 0.001$ (left) and $p = 0.18$ (right).

See also Figure S2, Videos S2 and S3, and Data S1.

bifurcation could occur in a self-sustaining manner without mesenchymal cells. The quantification of the ERK activity and tissue curvature at the tip apex shows that the decrease in ERK activity follows that in curvature (Figure 2E), with average delay of 97 min and the standard deviation of 21 min (Figure 2F). This observation allowed us to hypothesize that the ERK activity would be controlled by the curvature of the epithelial cells.

To clarify the morphological differences in cells between the convex and concave regions of epithelial tissues, we measured the basal and apical areas of epithelial cells through whole-tissue

CellPress
OPEN ACCESS

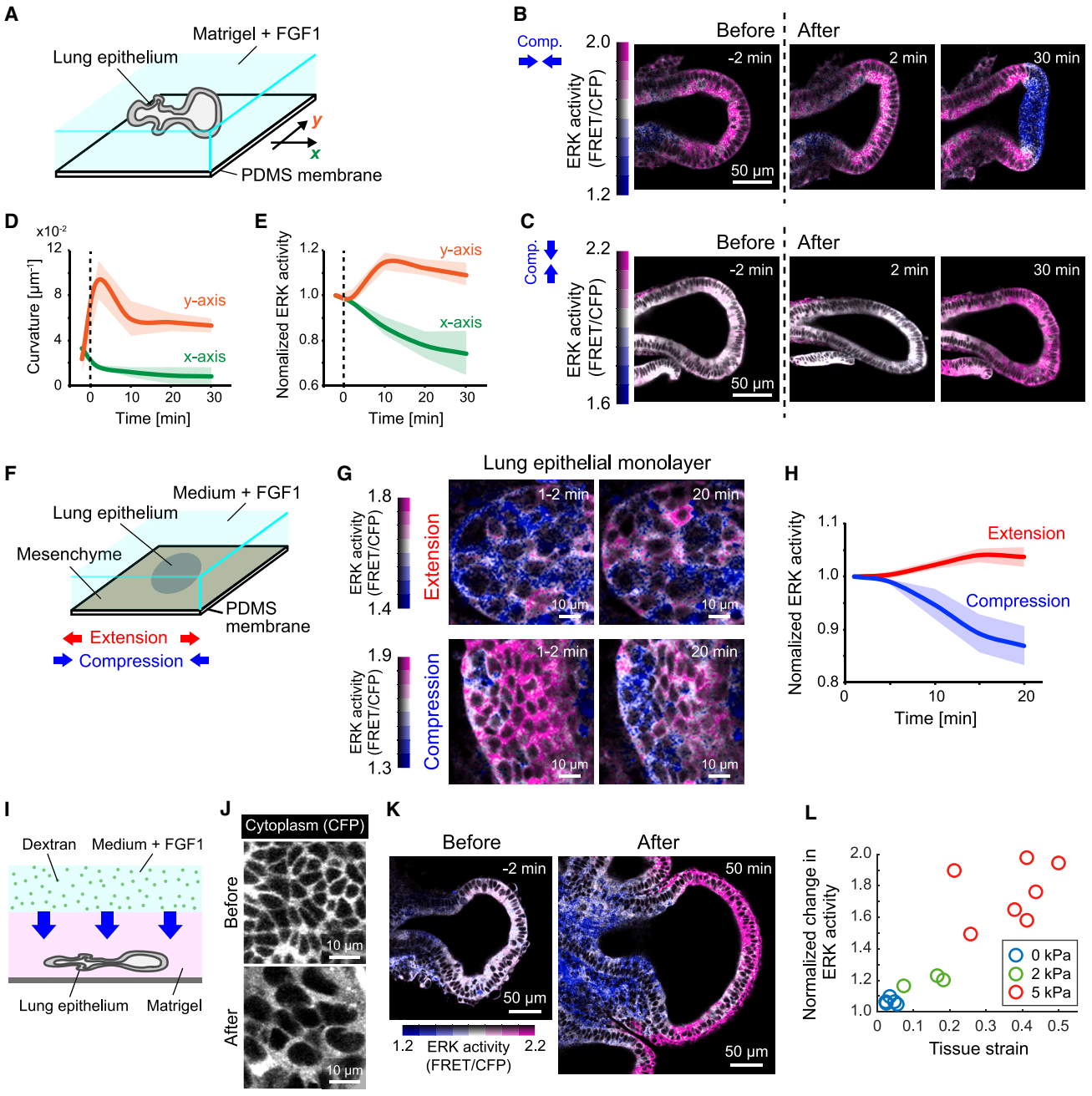

Figure 3. Response of ERK activity to mechanical perturbations

(A) Schematics of PDMS-based uniaxial compression assay performed on an isolated epithelium under the 3D culture condition. The x and y axes indicate directions parallel and vertical to the proximo-distal axes of the epithelium, respectively.

(B and C) Time-lapse images of the ERK activity for parallel compression (B) and vertical compression (C). Note that the color bar ranges, which indicate ERK activity, differ between (B) and (C) to effectively represent the change in ERK activity before and after the perturbation in each respective condition. Time origin indicates the timing of mechanical compression. Scale bars, 50 μm.

(D and E) Tissue curvature at the tip apex (D) and normalized ERK activity to the values at the initial time point (2 min prior to the perturbation) (E) over time. Colors represent the axes of compression, as shown in (A). Data represent mean and SD values. N = 3.

(F) Schematics of PDMS-based uniaxial mechanical perturbations under the 2D culture condition.

(G) Time-lapse images of the ERK activity in the isolated lung epithelium for the extension (upper) and compression (lower). Time origin indicates the timing of mechanical perturbations. Note that both sets of images in each extension and compression case show the cellular responses following mechanical perturbation, not before and after the perturbation. Scale bars, 50 μm.

(H) Normalized ERK activity to the values obtained at the initial time point (1–2 min after the perturbations) for the extension (red) and the compression (blue) processes over time. Data represent mean and SD values. N = 3.

(legend continued on next page)

staining using E-cadherin. The basal cell area of isolated epithelial tissues in the convex region was significantly larger than that in the concave region, whereas the apical cell area in the convex region was almost equivalent to that in the concave region (Figures 2G–2I). The epithelial basal edges act as an interface for cells to receive growth factor signals from external environments that activate ERK (Figure S2A). Therefore, we speculate that the extension of basal membranes would trigger ERK activation in the convex regions of epithelial tissues.

Morphological change of the epithelial tissues controls the ERK activity

To test whether the shape of epithelial tissues controls the ERK activity, we performed a physical perturbation assay using isolated epithelial tissues. We embedded isolated epithelial tissues within the FGF1-containing Matrigel filled inside a polydimethylsiloxane (PDMS) chamber, and uniaxially compressed it by 33% either parallelly or vertically to the distal-proximal axis of the lung epithelium (Figure 3A). Time-lapse images obtained during this process enable us to examine the ERK activity response to perturbations in different axes (Figures 3B and 3C). For parallel compression, the curved epithelial tissues at the tip apex became flattened (Figure 3D), and ERK activity decreased exclusively in the flat region (Figure 3E; Video S4A). However, for vertical compression, the tip apex of the epithelium became sharp (Figure 3D) and ERK activation followed the change in tissue curvature (Figure 3E; Video S4B).

We further examined the ERK activity response to cell deformation. The manipulation of cell shape in curved epithelial tissues remains unfeasible under 3D culture conditions; thus, we performed a strain perturbation assay under planar culture conditions using dissociated lung epithelial cells (Figure 3F). Under planar culture conditions, the stretching of cells led to ERK activation, whereas their compression led to ERK inactivation (Figures 3G and 3H). In addition, we performed osmolyte-based compression assay,[29] in which the Matrigel shrinks due to the difference in osmotic pressure with the culture medium (Figure 3I). The treatment with dextran molecules, acting as the osmolyte, resulted in the global compression from the top, leading to a flattening of the lung epithelial cells (Figure 3J). We found that ERK was significantly increased in the tips, which of the epithelium were extended on the plane orthogonal to the compression axis (Figure 3K). Remarkably, the ERK activation exhibited a positive correlation with the level of tissue extension in the tips (Figure 3L). Together, these results suggest that the strain on the cell area would be key to curvature-dependent ERK activity regulation. Notably, the surface area of the basal side of cells was significantly larger in the convex region with high ERK activity than in the concave region with lower ERK activity (Figure 2G). In summary, epithelial tissue curvature controls the ERK activity in cells, most likely through the strained state of their basal membranes.

ERK activation determines the epithelial cell shape via actin polymerization at the apical side

Next, we investigate how the ERK activity contributes to epithelial morphology and mechanics. We observed the change in the cell shape of isolated epithelial tissues treated with the MEK inhibitor PD0325901. Drug treatment led to an inhibition in the ERK activity within 30 min after administration (Figure S3A), and the apico-basal length of epithelial cells became longer than that observed in the control within 2 h (Figure 4A; Video S5). Hereafter, we refer to the apico-basal length of cells as the cell height and the cell length orthogonal to the apico-basal axis as the cell width (Figure 4B). ERK inactivation in cells treated with PD0325901 lengthened the cell height to 124% and shortened the cell width to 92% on an average, despite no significant changes in the cell size, compared with mock-treated cells (Figure 4C). This trend is consistent with that observed in the dissected murine lungs (Figures 1E–1G). These results indicate that the ERK activity regulates the cell height while maintaining the cell size.

To explore what causes the cell shape to change mechanically, we performed inhibitor assays on cytoskeletons, such as actin, microtubule, and non-muscle myosin, which allowed us to determine the mechanical contributions of targeted cytoskeletons to the cell morphology. As inferred by our theoretical analysis (see apical length vs cell height at equilibrium in method details), the cell height and the cell width showed an inverse relationship in the phase before cytoskeletal collapse, although it failed in the later phase owing to actin polymerization inhibition (Figure S3B). In addition, the cell width is not the parameter that can be measured robustly due to technical reasons of live imaging. Thus, we focused on the change in the cell height as a proxy for cytoskeletal perturbations. The cell height was increased markedly upon treatment with latrunculin A or cytochalasin D, each an inhibitor of actin polymerization, as observed in inhibiting ERK activity with PD0325901; conversely, the cell height was decreased by treatment with jasplakinolide, which promotes actin polymerization (Figures 4D and 4E). Because F-actin remarkably accumulated at the apical side of cells (Figure S3C), we speculated that actin polymerization at the apical edge would contribute to cell width extension by pushing the neighboring cells,[30] leading to the shortening of the cell height. To further analyze the mode of actin polymerization, we used CK-666, an Arp2/3 complex inhibitor, and SMIFH2, an inhibitor of the formin homology 2 domain. We found that the cell height was lengthened by CK-666 treatment but slightly shortened by SMIFH2 treatment (Figure 4E), suggesting that actin polymerization would depend on the Arp2/3-mediated nucleation of

(I) Schematics of osmolyte-based uniaxial compression assay from the top under the 3D culture condition. Blue arrows represent the displacement of interface between the Matrigel and the osmolyte-containing culture medium due to the gel shrinkage.
(J) Chang in cell size between before and after the treatment of the osmolyte. The cyan fluorescent protein (CFP) signal is localized in the cytoplasm. Scale bars, 10 μm.
(K) Snapshots of the ERK activity in the isolated lung epithelium before and after the osmolyte-based compression (lower). Scale bars, 50 μm.
(L) Normalized ERK activity to the values obtained before the treatment of the osmolyte versus the tissue strain in the distal tip. The data were obtained at 50 min after the dextran treatment. N = 5, 3, and 7 for 0, 2, and 5 kPa, respectively.
See also Figure S3, Videos S4 and S5, and Data S1.

CellPress
OPEN ACCESS

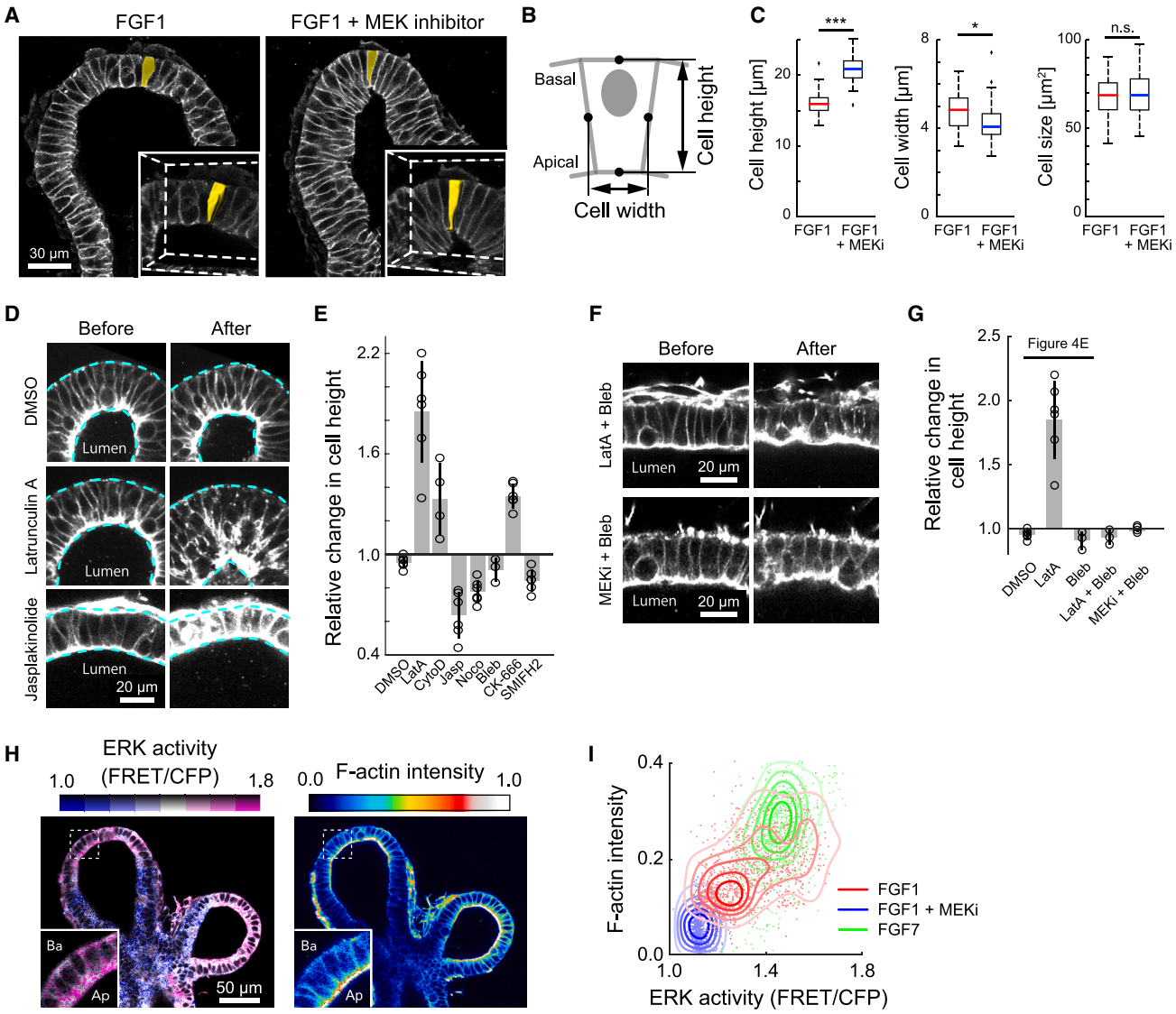

Figure 4. Response of cell morphology to chemical perturbations

(A) Change in the cell shape of an isolated epithelium upon treatment with either 500 ng mL^{-1} FGF1 (left) or the mixture of 500 ng mL^{-1} FGF1 and 1 μM PD0325901. The whole-mount immunofluorescence of anti-E-cadherin was used for the visualization. The inset windows represent the magnified 3D rendering focusing on a representative single cell marked in yellow. Scale bars, 30 μm.

(B) Schematics for cellular morphological measurement.

(C) Quantification of cell morphological parameters, including cell height, width, and size. n = 60, N = 3. Welch's t test, $p < 0.001$ (left), $p = 0.013$ (middle), and $p = 0.4$ (right).

(D) Change in the cell morphology of an isolated epithelium upon treatment with either DMSO control, 1 μM latrunculin A, or 1 μM jasplakinolide. SiR-actin, a F-actin labeling probe, was used for visualization. Scale bars, 20 μm.

(E) Relative change in the cell height upon the inhibitor treatment for cytoskeletons. Concentrations of inhibitors: 1 μM Latrunculin A, 1 μM cytochalasin D, 1 μM nocodazole, 30 μM blebbistatin, 1 μM jasplakinolide, 100 μM CK-666, and 10 μM SMIFH2. The bar graph and error bars represent mean and SD values. N ≥ 3 for each treatment.

(F) Snapshots of the cell morphology before and 40 min after the treatment with either the mixture of 1 μM latrunculin A and 30 μM blebbistatin or the mixture of 1 μM PD0325901 (MEK inhibitor) and 30 μM blebbistatin. The SiR-actin was used for visualization. Scale bars, 20 μm.

(G) Relative change in the cell height upon the inhibitor treatment for cytoskeletons. The three on the left are the same as (E) and shown for a comparison purpose. The bar graph and error bars represent mean and SD values. N = 3 and 4 for LatA + Bleb and MEKi + Bleb, respectively.

(H) Spatial map of ERK activity and F-actin accumulation level visualized by SiR-actin labeling upon treatment with 500 ng mL^{-1} FGF1. Inset windows show magnified views that focus on their subcellular localization. Ap, apical; Ba, basal. Scale bars, 50 μm.

(I) Scatterplot and contour map of ERK activity in the cytoplasm and F-actin intensity at the apical edge. Colors indicate the administration of different chemicals; red: 500 ng mL^{-1} FGF1, n = 1,204, N = 4 (representative images are available in H), blue: 500 ng mL^{-1} FGF1 and 1 μM PD0325901 (MEKi), n = 687, N = 3, green: 100 ng mL^{-1} FGF7, n = 787, N = 3.

See also Data S1.

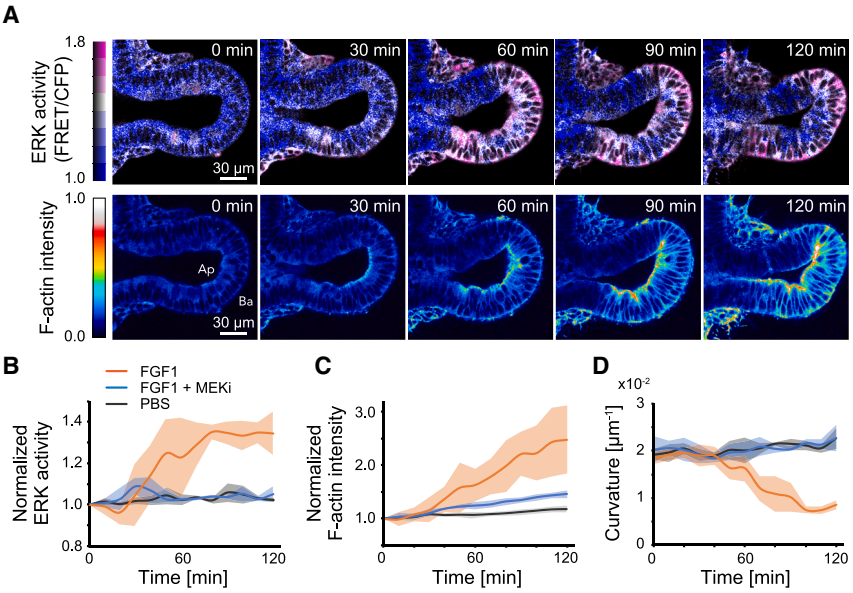

Figure 5. Simultaneous imaging of FGF-triggered ERK activation, actin polymerization, and tissue flattening

(A) Time-lapse images of ERK activity (upper) and F-actin intensity (lower). SiR-actin was pretreated for F-actin visualization, 1 h before the addition of FGF1. The time origin indicates the timing of FGF1 administration. Ap, apical; Ba, basal. Scale bars, 30 μm.

(B–D) Normalized ERK activity in the tips (B), normalized F-actin intensity in the tips (C), and tissue curvature at the tip apex (D) over time. Colors indicate different chemical treatments, including with 500 ng mL^{-1} FGF1 and 1 μM PD0325901 (MEKi). The time origin indicates the timing of chemical administration. Data represent mean and SD values. N = 4 for (B) and N = 3 for (C and D).

See also Figure S4, Video S6, and Data S1.

branched filaments, rather than formin-mediated actin nucleation.

The cell height was also shortened by interfering with microtubule polymerization with nocodazole; combined treatment with nocodazole and latrunculin A resulted in significant cell height extension via the rupture of lateral cell edges (Figures S3D and S3E). Microtubules within the lung epithelial cells are distributed along the apico-basal axis (Figure S3F) and would thus stabilize the cytoskeletal architecture cooperatively with F-actin. The inhibition of the activity of non-muscle myosin II with blebbistatin resulted in no significant difference in cell height, compared with that observed with DMSO control (Figure 4E). Active myosin localized at the apical edges in the tips of lung epithelium despite a weak level of accumulation (Figures S3G–S3G″). Moreover, blebbistatin treatment suppressed the cell elongation triggered by latrunculin A (Figures 4F and 4G). Taken together, these results indicate that contractile squeezing of apical edges drives apico-basal cell elongation only under the inhibitory situation of actin polymerization. Importantly, treatment with the combination of blebbistatin and PD0325901 resulted in suppression of the cell elongation as in the case of combined treatment with blebbistatin and latrunculin A (Figures 4F and 4G).

We speculated that ERK activation promoted F-actin accumulation within cells. This proposition is grounded in our observation that the inhibition of ERK activity and actin polymerization produced analogous effects on cell height. Furthermore, this hypothesis finds support in previous studies, which have revealed that ERK directly phosphorylates key regulatory proteins, such as WAVE2, Abi1, and cortactin, playing roles in the nucleation and regulation of actin polymerization.[31–33] Simultaneous imaging for the two factors revealed that F-actin accumulated at the apical side of cells exclusively in the tips where ERK activation occurred, under FGF1-treated conditions (Figure 4H). Mapping between the ERK activity and F-actin accumulation level via 3D whole-tissue imaging clearly showed a positive correlation with FGF1 (ρ = 0.51), although the inhibition of the ERK activity led to a significant decrease in the F-actin accumulation at the apical side of cells throughout the epithelial tissues, and relatively uniform distribution (Figure 4I). In addition, treatment with FGF7, which activates ERK globally in the isolated epithelial tissues regardless of the tissue curvature (Figures 2C and S2D), led to an increase in the apical F-actin accumulation overall throughout the epithelial tissues (Figure 4I). Thus, we found that ERK activation promotes actin polymerization at the apical edges of cells, and ultimately controls the cellular shape in the epithelial monolayer.

ERK activation flattens the epithelium via the apical actin polymerization

How does the ERK-mediated actin polymerization at the apical side of cells result in morphological changes in monolayer tissues? To answer this, we used a simple geometrical model of a two-dimensional monolayer tissue, composed of cells with identical morphologies. In this model, individual cells are represented by tetragons, the edges of which each correspond to the apical, basal, and lateral sides of cells. Then, the sheet curvature κ can be represented as a function of the length of these edges; especially, a change in the curvature with respect to the apical edge length a can be derived as $\partial\kappa/\partial a < 0$. Thus, the sheet curvature decreases with an expansion in the apical edge (see apical length vs epithelial sheet curvature in method details). This theoretical analysis, combined with the observation of ERK-dependent actin polymerization (Figures 4H and 4I), suggests that ERK activation would lead to a reduction in tissue curvature through actin polymerization at the apical edges

To confirm this hypothesis, we examined the change in epithelial tissue curvature in response to acute ERK activation. For this purpose, an isolated lung epithelium embedded in Matrigel was cultured in a growth factor-free medium, and subsequently, FGF1 was introduced into the medium to simulate ERK activity. The acute ERK activation promoted F-actin accumulation exclusively at the apical side of cells in epithelial distal tips, followed by the flattening of the epithelial sheet (Figures 5A–5D; Video S6). The simultaneous administration of FGF1 and the MEK inhibitor PD0325901 resulted in neither F-actin accumulation nor tip flattening; this was also observed for the solvent

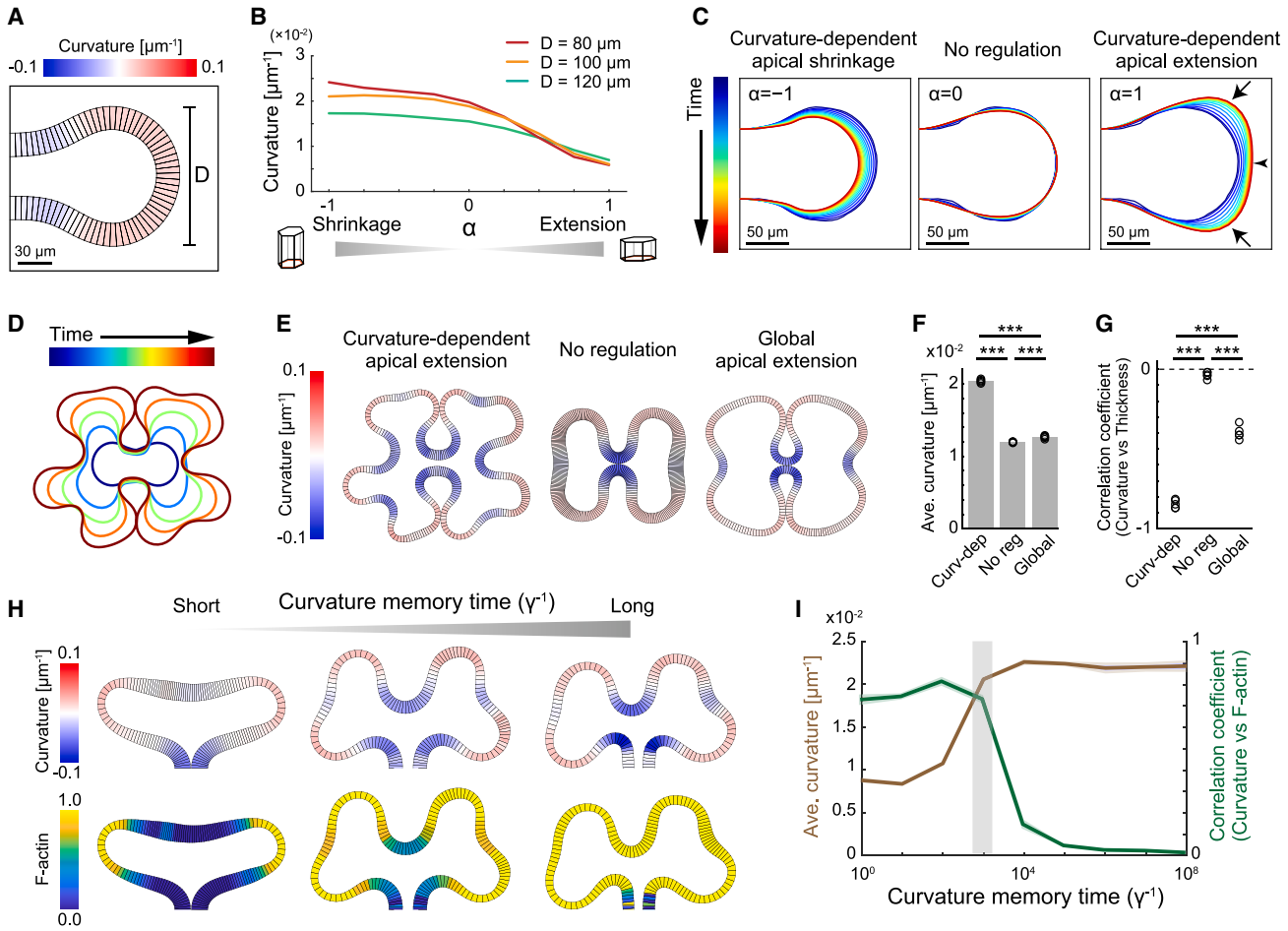

Figure 6. Simulation and analysis of the mathematical model

(A) Distal tip of a virtual epithelial monolayer tissue during the initial configuration of the simulation. Colors indicate the tissue curvature. D represents the diameter of the tip. Scale bars, 30 μm.

(B) Tissue curvature at the tip apex over the parameter α. Colors indicate the tip diameter.

(C) Time evolution of the basal sides of cells in different α. Colors indicate the time periods in simulations. The arrowhead indicates the tip apex, and arrows indicate the regions with a growing curvature. Scale bars, 50 μm.

(D) Time evolution of the basal sides of cells in the simulation with cell proliferation at $\alpha = 1$.

(E) Generated morphology of epithelial monolayer tissues in different regimes. Curvature-dependent apical extension: $\alpha = 1$, $\beta = 0$; no regulation: $\alpha = 0$, $\beta = 0$; global apical extension: $\alpha = 0$, $\beta = 0.2$.

(F and G) Averaged curvature (F) and correlation coefficient between the tissue curvature and tissue thickness (G) for the 3 regulatory regimes. Bars represent mean values. N = 5. Welch's t test, $p < 0.001$.

(H) Spatial maps of the curvature (upper) and F-actin level (lower) for different curvature memory time periods γ^{-1}. left: $\gamma = 1$, middle: $\gamma = 10^{-3}$, right: $\gamma = 10^{-6}$.

(I) Tissue curvature (green) and correlation coefficient between the curvature and the F-actin level. Data represent mean and SD values. N = 5. The gray shaded region indicates the region in which both the values are high.

See also Figures S5 and S6, Video S7, and Data S1.

control treatment (Figure S4A). Furthermore, the reduction in tissue curvature at the distal tips was also observed through the promotion of actin polymerization with jasplakinolide (Figure S4B). These results indicate that ERK activation flattens the epithelial tissues in the tips via actin polymerization at the apical sides of cells.

Feedback between ERK activity and tissue curvature explains repetitive branching

Finally, we performed numerical analysis using vertex dynamics model, a cell-based mechanical model,[34–36] to examine whether the curvature-dependent apical extension is able to produce the periodic branching pattern. The model represents epithelial cells as polygons with vertices and edges, and the edges on the apical side actively deform via F-actin dynamics that depend on the tissue-scale curvature and its decay. We conducted numerical simulations with an initial shape and bud diameters obtained from the experiment (Figure 6A) and examined the impact of curvature on the change in apical edge length through a model parameter α, using the standardized parameter set (Figure S5A). The apical edge extends/shrinks in accordance with the positive/negative values of α

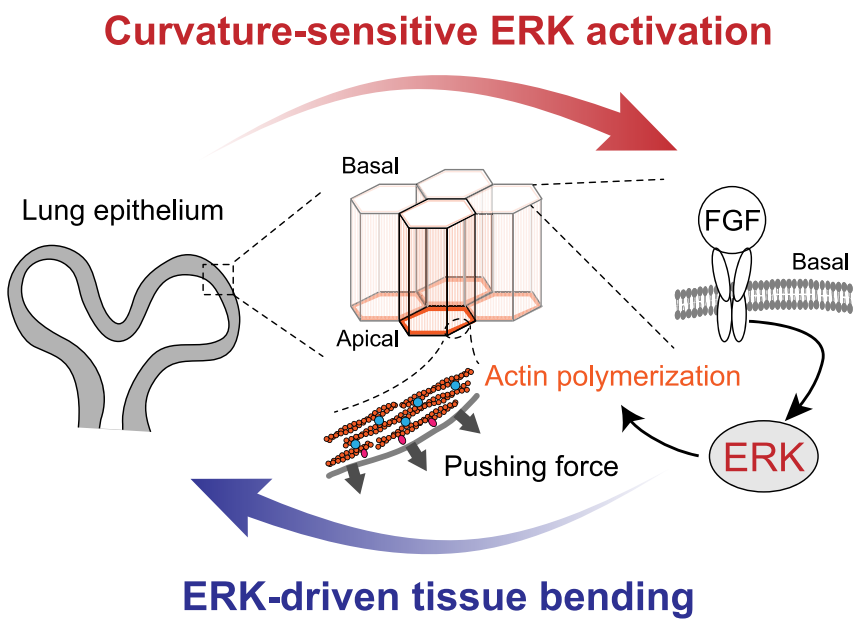

Figure 7. ERK-mediated curvature feedback regulates branching morphogenesis in murine lung epithelial tissue

The epithelial cells activate ERK specifically in tissues with a positive curvature via reception of extracellular FGF ligands (red arrow). ERK-mediated actin polymerization contributes to the extension of the apical side of cells, which decreases the tissue curvature (blue arrow). Thus, there is a closed negative feedback loop between tissue curvature and ERK activity across multiple scales in developing epithelial lung tissues.

in a curvature-dependent manner (Figure 6B). Clearly, the curvature and cell height at the tip apex decreased with an increase in α at equilibrium (Figures 6B and S5B). Moreover, during curvature-dependent apical extension ($\alpha = 1$), the curvature decreases at the tip apex (arrowhead, Figure 6C) but increases at both sides over time (arrows, Figure 6C), indicating that the curvature-dependent apical extension can create new buds for terminal bifurcation. This does not happen in the opposite case ($\alpha = -1$), suggesting that curvature-dependent apical constriction is not likely to drive repetitive branching, contradictory to a previous report.[37]

We then enabled cell proliferation to occur in the model system, to perform *in silico* experiments in virtual growing monolayer tissues. The simulation of the regime of curvature-dependent apical extension and cell proliferation (Figure S6) clearly demonstrates the formation of repetitive branching patterns (Figure 6D; Video S7A). In contrast, the repetitive branching pattern is not generated in counterpart regimes, such as no regulation on the apical edge, and global apical extension as observed for the FGF7 treatment—apical extension happens in all cells, irrespective of curvature (Figure 6E). In these counterpart regimes, there are significant differences in both the averaged curvature, a measure of curvature averaged over the entire tissue, and the correlation coefficient between the curvature and monolayer thickness (Figures 6F and 6G). Moreover, the virtual experiments show that luminal pressure, which has been proposed to be a physical factor for lung morphogenesis,[38,39] is not essential for branching pattern formation; rather, it suppresses its constant large magnitude value (Figure S5C). These results support the fact that the exclusive occurrence of apical edge extension in cells with high curvatures drives repetitive terminal bifurcation in the growing epithelial monolayer in a self-sustaining manner.

Furthermore, numerical investigations have clarified that the retention time of curvature memory in F-actin, i.e., the inverse of the F-actin decay rate γ, is crucial for generating the branching pattern (Figure 6H; Video S7B). The averaged curvature becomes larger for a longer curvature memory, and the correlation between the curvature and F-actin becomes higher for a shorter curvature memory. Thus, there is an optimal range for the retention time of the curvature memory in F-actin (Figure 6I). This result predicts the importance of the tissue curvature hysteresis of cellular force generation via F-actin, for the emergence of repetitive branch patterns.

DISCUSSION

We have demonstrated a regulatory mechanism by which epithelial monolayer cells undergo repetitive branching morphogenesis through curvature sensing and ERK-mediated mechanical force generation in a self-sustained manner. Our two-photon live imaging analysis has shown that the ERK activity changes following a dynamic change in the tissue curvature, and ERK activation occurs preferentially in the curved region of epithelial tissues. Moreover, we found that ERK-mediated actin polymerization contributes to the lateral extension of the apical side of cells. Finally, we demonstrated its importance for achieving a decrease in tissue curvature during terminal bifurcation via mathematical model analyses. Thus, we propose a negative feedback loop between the tissue curvature and ERK activity across multiple scales underlies the morphogenesis of developing lung epithelial tissues (Figure 7).

The results presented in this study provide a better understanding of lung epithelial branching, in conjunction with previously determined theory-based mechanisms, based on mechanical and chemical aspects. From a mechanical viewpoint, it has been proposed that the spatial patterning of the isolated lung epithelium arises from the proliferation-induced physical instability of the epithelial layer, known as mechanical buckling,[40] in various developing epithelial tissues.[1,41,42] This purely mechanical model may explain the formation of an initial branching pattern under the assumption that the epithelial tissue acts as an elastic layer but requires the physical conditions under which mechanical buckling occurs. However, our results have demonstrated that repetitive branching can be generated even at a range where proliferation-induced buckling does not occur (Figures 6E–6G). We emphasize that the regime presented here is not mutually exclusive to buckling-induced patterning. Thus, ERK-mediated tissue curvature feedback results in a

robust regulatory system underlying branching morphogenesis, together with the buckling regime. In addition, a simple reaction-diffusion model of substrate depletion has been proposed for integrating chemical signals and tissue growth[43,44]; the model assumes that lung epithelial cells consume FGF ligands that have slow diffusion rates and thereby predicts that a concentration gradient of FGF should be generated in the extracellular matrix. However, our live imaging analysis results have shown that no FGF gradient was formed in the Matrigel, whereas FGF was internalized in the epithelial cells through endocytosis (Figure S2). Other reaction-diffusion systems have focused on genetic regulatory networks that can achieve the localization of *Fgf10* expression observed *in vivo*.[45–47] Although the spatial distribution of the chemoattractant is dispensable for epithelial branching[17] (Figures 2B–2D), the incorporation of such fundamental biochemical signals into our model would be useful for studying detailed systems for lung branching and patterning *in vivo*.

Our findings highlight the curvature-sensitive ERK activation of lung epithelial cells and raise an issue on how cells sense the tissue curvature and transmit FGF-ERK signals. Because the ERK activity response occurred within 10 min after the mechanical perturbation in the tissue curvature (Figures 3B–3E), the feedback regulation via gene expression, e.g., the interplay between the *Fgfs*, *Sonic hedgehog*, and *Sprouty* expressed in the epithelium, are unlikely. Rather, we surmise that both ERK activation and inhibition processes involve unknown protein-protein interactions. We propose that the phenomenon of curvature-sensitive ERK activation in lung epithelial tissues can be attributable to the strain of the basal membrane (Figures 2G–2I and 3G–3K). Moreover, an extension of the basal membrane would trigger receptor-mediated endocytosis because the FGF internalization occurred exclusively in the epithelial tissues with positive curvature (Figure S2). Mechanical stretching or relaxing is recognized to modulate membrane tension, subsequently influencing endocytosis and ERK activity. For instance, reduced membrane tension in mouse stem cells prompts heightened endocytosis of FGF signaling components, thereby triggering ERK activation.[48] Distinct ERK responses to various FGFs in the lung epithelium could be a result of the ligand-dependent trafficking of FGF receptors. For instance, when simulating FGF10 for FGFR2b, the receptor internalizes and subsequently recycles, whereas FGF7 triggers FGFR2b degradation, through modulating the duration of activation of adaptor proteins, such as FRS2 and SHC, in mammalian cell lines.[49,50] Extensive analysis integrating intracellular events involving FGFR endocytic trafficking and plasma membrane curvature sensing will enhance our understanding of this process. Further exploration to delineate the influence of strain of the basal membrane on the endocytosis and ERK activity is necessary, alongside the development of appropriate methodologies.

One remaining question pertains to the mechanisms by which ERK activation triggers actin polymerization specifically at the apical side of epithelial cells. Earlier studies have shown direct interactions between ERK and actin polymerization regulators, such as WAVE2, Abi1, and cortactin,[31,33] along with evidence of ERK activation inducing actin polymerization in diverse epithelial cell types.[30,32,51] Still, the specifics of how ERK is recruited to the apical side of cells remain unclear. Clarifying detailed regions of ERK activation is pivotal for understanding this process, although it currently poses a challenge due to the diffuse nature of the FRET biosensor used in this study. Further technological advancements are required to visualize the interaction between ERK and actin polymerization regulators at subcellular resolutions.

This study has focused on the core mechanism to minimally generate the self-sustained repetitive branching patterns in epithelium; however, there are other additional contributions that could achieve the robust tissue morphogenesis *in vivo*. For example, smooth muscle cells are not necessary for the initiation of cleft formation (Figure 2D)[52] but should mechanically assist the cleft formation from the outside of an epithelium, realizing the stable terminal branching.[26,52,53] Moreover, fibronectin, a target of Wnt signaling, plays a pivotal role in cleft formation during the initiation of epithelial branching in the murine lung. Decreased fibronectin levels through DKK1, a negative regulator of Wnt signaling, correlate with reduced branching in the lung epithelium, suggesting the involvement of canonical Wnt signaling and its potential impact on smooth muscle cell differentiation.[54] Luminal fluid is another potentially critical factor that can mechanically affect epithelial tissue deformation through shear stress and hydrostatic pressure.[55] It has been previously reported that the manipulation of luminal pressure in murine developing lungs under *ex vivo* culture conditions altered branch formation.[38] Because oscillatory contractions of airway smooth muscles are likely to produce dynamic changes in the luminal pressure, it has been suggested that rhythmic luminal pressure would control the global synchronization of branching events in the murine lung,[39] although it does not contribute to the tissue flattening during the terminal bifurcation.

The ERK-mediated curvature feedback mechanism proposed here advances the concept of mechano-chemical regulation of the epithelial monolayer,[35,56–58] in terms of taking the impact of tissue geometry into account. In various tissues, the epithelial cells collectively form their shape in the tissue scale and the constituent cells respond to the tissue curvature at different levels, including the transcription and cell activity levels.[59–62] We believe that the proposed system works as a regulatory design principle underlying the mechanisms of self-organized tissue morphogenesis.

STAR★METHODS

Detailed methods are provided in the online version of this paper and include the following:

- KEY RESOURCES TABLE
- RESOURCE AVAILABILITY
  - Lead contact
  - Materials availability
  - Data and code availability
- EXPERIMENTAL MODEL AND SUBJECT DETAILS
  - Animals
- METHOD DETAILS
  - Antibodies, small molecules, and recombinant proteins
  - *Ex vivo* culture
  - Whole-tissue immunofluorescence staining
  - F-actin and tubulin labeling

- Fluorescence labeling of FGF
- Ethynyl deoxyuridine (EdU) assay
- Microscopy
- Mechanical strain assay
- Osmolyte-based compression assay
- Mathematical modeling and analysis

- QUANTIFICATION AND STATISTICAL ANALYSIS
  - FRET image analysis
  - Three-dimensional mapping
  - Curvature measurement in 2D
  - Statistical hypothesis testing
  - Graph

SUPPLEMENTAL INFORMATION

Supplemental information can be found online at https://doi.org/10.1016/j.cub.2023.12.049.

ACKNOWLEDGMENTS

This work was supported by JST PRESTO grant JPMJPR1949, JSPS KAKENHI 19H00993 and 21H05290, the Medical Research Support Center of Kyoto University, and the Mechanobiology Institute (MBI) at the National University of Singapore funded through the National Research Foundation, Singapore and the Ministry of Education, Singapore under the Research Centre of Excellence program and by the Department of Physiology at the National University of Singapore. We would like to thank Yu Kurata and Akane Kusumi for technical assistance and Edouard Hannezo, Naoya Hino, Mamoru Ishii, and Takuya Yoshida for fruitful discussion.

AUTHOR CONTRIBUTIONS

Conceptualization, T.H.; methodology, T.H. and M.M.; software, T.H.; validation, T.H.; formal analysis, T.H.; investigation, T.H.; resources, T.H. and M.M.; data curation, T.H.; writing – original draft, T.H.; writing – review & editing, T.H. and M.M.; visualization, T.H.; supervision, T.H.; project administration, T.H.; funding acquisition, T.H.

DECLARATION OF INTERESTS

The authors declare no competing interests.

Received: July 14, 2022
Revised: November 6, 2023
Accepted: December 14, 2023
Published: January 15, 2024

REFERENCES

1. Hirashima, T. (2014). Pattern formation of an epithelial tubule by mechanical instability during epididymal development. Cell Rep. *9*, 866–873.
2. Metzger, R.J., Klein, O.D., Martin, G.R., and Krasnow, M.A. (2008). The branching programme of mouse lung development. Nature *453*, 745–750.
3. Hannezo, E., Scheele, C.L.G.J., Moad, M., Drogo, N., Heer, R., Sampogna, R.V., van Rheenen, J., and Simons, B.D. (2017). A unifying theory of branching morphogenesis. Cell *171*, 242–255.e27.
4. Cardoso, W.V., and Lü, J. (2006). Regulation of early lung morphogenesis: questions, facts and controversies. Development *133*, 1611–1624.
5. Warburton, D., El-Hashash, A., Carraro, G., Tiozzo, C., Sala, F., Rogers, O., De Langhe, S., Kemp, P.J., Riccardi, D., Torday, J., et al. (2010). Lung organogenesis. Curr. Top. Dev. Biol. *90*, 73–158.
6. Herriges, M., and Morrisey, E.E. (2014). Lung development: orchestrating the generation and regeneration of a complex organ. Development *141*, 502–513.
7. Varner, V.D., and Nelson, C.M. (2014). Cellular and physical mechanisms of branching morphogenesis. Development *141*, 2750–2759.
8. Ingber, D.E. (2006). Mechanical control of tissue morphogenesis during embryological development. Int. J. Dev. Biol. *50*, 255–266.
9. Anlaş, A.A., and Nelson, C.M. (2018). Tissue mechanics regulates form, function, and dysfunction. Curr. Opin. Cell Biol. *54*, 98–105.
10. Ornitz, D.M., and Itoh, N. (2015). The fibroblast growth factor signaling pathway. Wiley Interdiscip. Rev. Dev. Biol. *4*, 215–266.
11. Cardoso, W.V., Itoh, A., Nogawa, H., Mason, I., and Brody, J.S. (1997). FGF-1 and FGF-7 induce distinct patterns of growth and differentiation in embryonic lung epithelium. Dev. Dyn. *208*, 398–405.
12. Nogawa, H., and Ito, T. (1995). Branching morphogenesis of embryonic mouse lung epithelium in mesenchyme-free culture. Development *121*, 1015–1022.
13. Bellusci, S., Grindley, J., Emoto, H., Itoh, N., and Hogan, B.L.M. (1997). Fibroblast growth factor 10 (FGF10) and branching morphogenesis in the embryonic mouse lung. Development *124*, 4867–4878.
14. Min, H., Danilenko, D.M., Scully, S.A., Bolon, B., Ring, B.D., Tarpley, J.E., DeRose, M., and Simonet, W.S. (1998). Fgf-10 is required for both limb and lung development and exhibits striking functional similarity to Drosophila branchless. Genes Dev. *12*, 3156–3161.
15. Sekine, K., Ohuchi, H., Fujiwara, M., Yamasaki, M., Yoshizawa, T., Sato, T., Yagishita, N., Matsui, D., Koga, Y., Itoh, N., et al. (1999). Fgf10 is essential for limb and lung formation. Nat. Genet. *21*, 138–141.
16. Arman, E., Haffner-Krausz, R., Gorivodsky, M., and Lonai, P. (1999). Fgfr2 is required for limb outgrowth and lung-branching morphogenesis. Proc. Natl. Acad. Sci. USA *96*, 11895–11899.
17. Volckaert, T., Campbell, A., Dill, E., Li, C., Minoo, P., and De Langhe, S. (2013). Localized Fgf10 expression is not required for lung branching morphogenesis but prevents differentiation of epithelial progenitors. Development *140*, 3731–3742.
18. Boucherat, O., Nadeau, V., Bérubé-Simard, F.A., Charron, J., and Jeannotte, L. (2015). Crucial requirement of ERK/MAPK signaling in respiratory tract development. Development *142*, 3801.
19. Yoshida, T., Matsuda, M., and Hirashima, T. (2020). Incoherent feedforward regulation via Sox9 and ERK underpins mouse tracheal cartilage development. Front. Cell Dev. Biol. *8*, 585640.
20. Jiang, K., Tang, Z., Li, J., Wang, F., and Tang, N. (2018). Anxa4 mediated airway progenitor cell migration promotes distal epithelial cell fate specification. Sci. Rep. *8*, 14344.
21. Liu, Y., Stein, E., Oliver, T., Li, Y., Brunken, W.J., Koch, M., Tessier-Lavigne, M., and Hogan, B.L.M. (2004). Novel role for netrins in regulating epithelial behavior during lung branching morphogenesis. Curr. Biol. *14*, 897–905.
22. Tang, N., Marshall, W.F., McMahon, M., Metzger, R.J., and Martin, G.R. (2011). Control of mitotic spindle angle by the RAS-regulated ERK1/2 pathway determines lung tube shape. Science *333*, 342–345.
23. Komatsu, N., Terai, K., Imanishi, A., Kamioka, Y., Sumiyama, K., Jin, T., Okada, Y., Nagai, T., and Matsuda, M. (2018). A platform of BRET-FRET hybrid biosensors for optogenetics, chemical screening, and in vivo imaging. Sci. Rep. *8*, 8984.
24. Komatsu, N., Aoki, K., Yamada, M., Yukinaga, H., Fujita, Y., Kamioka, Y., and Matsuda, M. (2011). Development of an optimized backbone of FRET biosensors for kinases and GTPases. Mol. Biol. Cell *22*, 4647–4656.
25. Harvey, C.D., Ehrhardt, A.G., Cellurale, C., Zhong, H., Yasuda, R., Davis, R.J., and Svoboda, K. (2008). A genetically encoded fluorescent sensor of ERK activity. Proc. Natl. Acad. Sci. USA *105*, 19264–19269.
26. Kim, H.Y., Pang, M.F., Varner, V.D., Kojima, L., Miller, E., Radisky, D.C., and Nelson, C.M. (2015). Localized smooth muscle differentiation is essential for epithelial bifurcation during branching morphogenesis of the mammalian lung. Dev. Cell *34*, 719–726.
27. Yuan, T., Klinkhammer, K., Lyu, H., Gao, S., Yuan, J., Hopkins, S., Zhang, J.S., and De Langhe, S.P. (2020). Temporospatial expression of Fgfr1 and

2 during lung development, homeostasis, and regeneration. Front. Pharmacol. *11*, 120.

28. Amaya, E., Musci, T.J., and Kirschner, M.W. (1991). Expression of a dominant negative mutant of the FGF receptor disrupts mesoderm formation in Xenopus embryos. Cell *66*, 257–270.
29. Dolega, M.E., Monnier, S., Brunel, B., Joanny, J.F., Recho, P., and Cappello, G. (2021). Extracellular matrix in multicellular aggregates acts as a pressure sensor controlling cell proliferation and motility. eLife *10*, e63258.
30. Mendoza, M.C., Vilela, M., Juarez, J.E., Blenis, J., and Danuser, G. (2015). ERK reinforces actin polymerization to power persistent edge protrusion during motility. Sci. Signal. *8*, ra47.
31. Lavoie, H., Gagnon, J., and Therrien, M. (2020). ERK signalling: a master regulator of cell behaviour, life and fate. Nat. Rev. Mol. Cell Biol. *21*, 607–632.
32. Nayak, A.N., and Hirashima, T. (2023). Tug-of-war via ERK signaling pathway for tissue organization – ERK activation to force generation. Curr. Opin. Cell Biol. *85*, 102249.
33. Tanimura, S., and Takeda, K. (2017). ERK signalling as a regulator of cell motility. J. Biochem. *162*, 145–154.
34. Nagai, T., and Honda, H. (2001). A dynamic cell model for the formation of epithelial tissues. Philos. Mag. B *81*, 699–719.
35. Hirashima, T., and Adachi, T. (2019). Polarized cellular mechano-response system for maintaining radial size in developing epithelial tubes. Development *146*, dev181206.
36. Fletcher, A.G., Osterfield, M., Baker, R.E., and Shvartsman, S.Y. (2014). Vertex models of epithelial morphogenesis. Biophys. J. *106*, 2291–2304.
37. Fumoto, K., Takigawa-Imamura, H., Sumiyama, K., Kaneiwa, T., and Kikuchi, A. (2017). Modulation of apical constriction by Wnt signaling is required for lung epithelial shape transition. Development *144*, 151–162.
38. Unbekandt, M., del Moral, P.M., Sala, F.G., Bellusci, S., Warburton, D., and Fleury, V. (2008). Tracheal occlusion increases the rate of epithelial branching of embryonic mouse lung via the FGF10-FGFR2b-Sprouty2 pathway. Mech. Dev. *125*, 314–324.
39. Nelson, C.M., Gleghorn, J.P., Pang, M.F., Jaslove, J.M., Goodwin, K., Varner, V.D., Miller, E., Radisky, D.C., and Stone, H.A. (2017). Microfluidic chest cavities reveal that transmural pressure controls the rate of lung development. Development *144*, 4328–4335.
40. Varner, V.D., Gleghorn, J.P., Miller, E., Radisky, D.C., and Nelson, C.M. (2015). Mechanically patterning the embryonic airway epithelium. Proc. Natl. Acad. Sci. USA *112*, 9230–9235.
41. Kourouklis, A.P., and Nelson, C.M. (2018). Modeling branching morphogenesis using materials with programmable mechanical instabilities. Curr. Opin. Biomed. Eng. *6*, 66–73.
42. Savin, T., Kurpios, N.A., Shyer, A.E., Florescu, P., Liang, H., Mahadevan, L., and Tabin, C.J. (2011). On the growth and form of the gut. Nature *476*, 57–62.
43. Miura, T., and Shiota, K. (2002). Depletion of FGF acts as a lateral inhibitory factor in lung branching morphogenesis in vitro. Mech. Dev. *116*, 29–38.
44. Hartmann, D., and Miura, T. (2006). Modelling in vitro lung branching morphogenesis during development. J. Theor. Biol. *242*, 862–872.
45. Hirashima, T., Iwasa, Y., and Morishita, Y. (2009). Mechanisms for split localization of Fgf10 expression in early lung development. Dev. Dyn. *238*, 2813–2822.
46. Menshykau, D., Kraemer, C., and Iber, D. (2012). Branch mode selection during early lung development. PLoS Comput. Biol. *8*, e1002377.
47. Menshykau, D., Blanc, P., Unal, E., Sapin, V., and Iber, D. (2014). An interplay of geometry and signaling enables robust lung branching morphogenesis. Development *141*, 4526–4536.
48. De Belly, H., Stubb, A., Yanagida, A., Labouesse, C., Jones, P.H., Paluch, E.K., and Chalut, K.J. (2021). Membrane tension gates ERK-mediated regulation of pluripotent cell fate. Cell Stem Cell *28*, 273–284.e6.
49. Belleudi, F., Leone, L., Nobili, V., Raffa, S., Francescangeli, F., Maggio, M., Morrone, S., Marchese, C., and Torrisi, M.R. (2007). Keratinocyte growth factor receptor ligands target the receptor to different intracellular pathways. Traffic *8*, 1854–1872.
50. Francavilla, C., Rigbolt, K.T.G., Emdal, K.B., Carraro, G., Vernet, E., Bekker-Jensen, D.B., Streicher, W., Wikström, M., Sundström, M., Bellusci, S., et al. (2013). Functional proteomics defines the molecular switch underlying FGF receptor trafficking and cellular outputs. Mol. Cell *51*, 707–722.
51. Samson, S.C., Khan, A.M., and Mendoza, M.C. (2022). ERK signaling for cell migration and invasion. Front. Mol. Biosci. *9*, 998475.
52. Young, R.E., Jones, M.K., Hines, E.A., Li, R., Luo, Y., Shi, W., Verheyden, J.M., and Sun, X. (2020). Smooth muscle differentiation is essential for airway size, tracheal cartilage segmentation, but dispensable for epithelial branching. Dev. Cell *53*, 73–85.e5.
53. Goodwin, K., Lemma, B., Zhang, P., Boukind, A., and Nelson, C.M. (2023). Plasticity in airway smooth muscle differentiation during mouse lung development. Dev. Cell *58*, 338–347.e4.
54. De Langhe, S.P., Sala, F.G., Del Moral, P.M., Fairbanks, T.J., Yamada, K.M., Warburton, D., Burns, R.C., and Bellusci, S. (2005). Dickkopf-1 (DKK1) reveals that fibronectin is a major target of Wnt signaling in branching morphogenesis of the mouse embryonic lung. Dev. Biol. *277*, 316–331.
55. Chan, C.J., and Hiiragi, T. (2020). Integration of luminal pressure and signalling in tissue self-organization. Development *147*, dev181297.
56. Boocock, D., Hino, N., Ruzickova, N., Hirashima, T., and Hannezo, E. (2021). Theory of mechanochemical patterning and optimal migration in cell monolayers. Nat. Phys. *17*, 267–274.
57. Hino, N., Rossetti, L., Marín-Llauradó, A., Aoki, K., Trepat, X., Matsuda, M., and Hirashima, T. (2020). ERK-mediated mechanochemical waves direct collective cell polarization. Dev. Cell *53*, 646–660.e8.
58. Ishii, M., Tateya, T., Matsuda, M., and Hirashima, T. (2021). Retrograde ERK activation waves drive base-to-apex multicellular flow in murine cochlear duct morphogenesis. eLife *10*, e61092.
59. Nikolaev, M., Mitrofanova, O., Broguiere, N., Geraldo, S., Dutta, D., Tabata, Y., Elci, B., Brandenberg, N., Kolotuev, I., Gjorevski, N., et al. (2020). Homeostatic mini-intestines through scaffold-guided organoid morphogenesis. Nature *585*, 574–578.
60. Nelson, C.M., VanDuijn, M.M., Inman, J.L., Fletcher, D.A., and Bissell, M.J. (2006). Tissue geometry determines sites of mammary branching morphogenesis in organotypic cultures. Science *314*, 298–300.
61. Luciano, M., Xue, S.-L., De Vos, W.H., Redondo-Morata, L., Surin, M., Lafont, F., Hannezo, E., and Gabriele, S. (2021). Cell monolayers sense curvature by exploiting active mechanics and nuclear mechanoadaptation. Nat. Phys. *17*, 1382–1390.
62. Hughes, A.J., Miyazaki, H., Coyle, M.C., Zhang, J., Laurie, M.T., Chu, D., Vavrušová, Z., Schneider, R.A., Klein, O.D., and Gartner, Z.J. (2018). Engineered tissue folding by mechanical compaction of the mesenchyme. Dev. Cell *44*, 165–178.e6.
63. Hirashima, T., and Adachi, T. (2015). Procedures for the quantification of whole-tissue immunofluorescence images obtained at single-cell resolution during murine tubular organ development. PLoS One *10*, e0135343.
64. Hirashima, T. (2020). Mechanical tissue compression and whole-mount imaging at single cell resolution for developing murine epididymal tubules. Bio Protoc. *10*, e3694.
65. Lukinavičius, G., Reymond, L., D'Este, E., Masharina, A., Göttfert, F., Ta, H., Güther, A., Fournier, M., Rizzo, S., Waldmann, H., et al. (2014). Fluorogenic probes for live-cell imaging of the cytoskeleton. Nat. Methods *11*, 731–733.
66. Milroy, L.G., Rizzo, S., Calderon, A., Ellinger, B., Erdmann, S., Mondry, J., Verveer, P., Bastiaens, P., Waldmann, H., Dehmelt, L., et al. (2012). Selective chemical imaging of static actin in live cells. J. Am. Chem. Soc. *134*, 8480–8486.
67. Monnier, S., Delarue, M., Brunel, B., Dolega, M.E., Delon, A., and Cappello, G. (2016). Effect of an osmotic stress on multicellular aggregates. Methods *94*, 114–119.

68. Hannezo, E., Prost, J., and Joanny, J.F. (2014). Theory of epithelial sheet morphology in three dimensions. Proc. Natl. Acad. Sci. USA *111*, 27–32.

69. Wen, F.L., Wang, Y.C., and Shibata, T. (2017). Epithelial folding driven by apical or basal-lateral modulation: geometric features, mechanical inference, and boundary effects. Biophys. J. *112*, 2683–2695.

70. Tran, A.P., Yan, S., and Fang, Q. (2020). Improving model-based functional near-infrared spectroscopy analysis using mesh-based anatomical and light-transport models. Neurophotonics *7*, 15008.

71. Meyer, M., Desbrun, M., Schröder, P., and Barr, A.H. (2003). Discrete differential-geometry operators for triangulated 2-manifolds. Comput. Aided Geom. Des. 35–57.

STAR★METHODS

KEY RESOURCES TABLE

REAGENT or RESOURCE	SOURCE	IDENTIFIER
Antibodies		
Rat monoclonal anti-E-cadherin	Cell Signaling Technology	Cat#3195; RRID: AB_2291471
Rabbit polyclonal anti-phospho-myosin light chain	Abcam	Cat#ab2480; RRID: AB_303094
Goat Alexa Fluor 546-conjugated anti-rat IgG (H+L)	Thermo Fisher Scientific	Cat#A11081; RRID: AB_2534125
Goat Alexa Fluor 647-conjugated anti-rabbit IgG (H+L)	Abcam	Cat#ab150079; RRID: AB_2722623
Goat Alexa Fluor 647-conjugated anti-rabbit IgG (H+L)	Thermo Fisher Scientific	Cat#A21247; RRID: AB_141778
Chemicals, peptides, and recombinant proteins		
Blebbistatin	Merck Millipore	Cat#203391
CK-666	Sigma-Aldrich	Cat#SML0006
Cytochalasin D	Merck Millipore	Cat#250255
Jasplakinolide	Abcam	Cat#ab141409
Latrunculin A	Cayman Chemical	Cat#10010630
Nocodazole	Merck Millipore	Cat#487928
PD0325901	FUJIFILM Wako Pure Chemical Corporation	Cat#162-25291
SMIFH2	Sigma-Aldrich	Cat#S4826
Y-27632	Merck Millipore	Cat#SCM075
FGF1	R&D Systems	Cat#232-FA
FGF7	R&D Systems	Cat#251-KG
Dispase I	FUJIFILM Wako Pure Chemical Corporation	Cat#386-02271
Growth factor-reduced Matrigel	Corning	Cat#356231
Dextran (1500-2800 kDa)	Merck Millipore	Cat#D5376
FluoroBrite DMEM Media	Thermo Fischer Scientific	Cat#A1896701
GlutaMAX	Thermo Fischer Scientific	Cat#35050061
Hoechst33342	Dojindo Molecular Technologies	Cat#H342
DAPI	Dojindo Molecular Technologies	Cat#D523-10
CUBIC-R+	Tokyo Chemical Industry	Cat#T3741
SiR-Actin	Cytoskeleton	Cat#CY-SC001
SiR-Tubulin	Cytoskeleton	Cat#CY-SC002
Collagenase/Dispase	Sigma-Aldrich	Cat#10269638001
KnockOut Serum Replacement	Thermo Fischer Scientific	Cat#10828010
Cellmatrix Type I-C (Collagen type1)	Nitta Gelatin	Cat#631-00771;
Critical commercial assays		
pHrodo iFL Red STP ester dye	Thermo Fischer Scientific	Cat#P36014
Alexa Fluor 488 Microscale Protein Labeling Kit	Thermo Fischer Scientific	Cat#A30006
Click-iT EdU Imaging Kits	Thermo Fisher Scientific	Cat#C10340
Deposited data		
Codes for the model simulations	This paper	https://github.com/tsuyoshihirashima/vertex-lung
Experimental models: Organisms/strains		
Mouse: hyBRET-ERK-NES	NIBIOHN	nbio325
Mouse: Slc:ICR	Japan SLC	RRID: MGI:5462094

(*Continued on next page*)

Continued

REAGENT or RESOURCE	SOURCE	IDENTIFIER
Software and algorithms		
Fiji	http://fiji.sc	RRID: SCR_002285
MATLAB	MathWorks; https://www.mathworks.com/	RRID: SCR_001622
IMARIS	Oxford Instruments; https://imaris.oxinst.com/	RRID: SCR_007370

RESOURCE AVAILABILITY

Lead contact

Further information and requests for resources and reagents should be directed to and will be fulfilled by the lead contact, Tsuyoshi Hirashima (thira@nus.edu.sg).

Materials availability

Materials developed for this study are available on request to the corresponding author.

Data and code availability

- Source data for all graphs are available in Data S1. Original data reported in this paper will be shared by the lead contact upon request.
- The original codes for the model simulations have been archived on GitHub and the DOI is listed in the key resources table.
- Any additional information required to re-analyze the data reported in this paper is available from the lead contact upon request.

EXPERIMENTAL MODEL AND SUBJECT DETAILS

Animals

It has been previously documented that transgenic mice manifested the expression of hyBRET-ERK-NES, a FRET biosensor conjoined with the nuclear export signal (NES) sequence.[23–25] The hyBRET-ERK-NES comprised cyan fluorescent protein (CFP) and yellow fluorescent protein (YFP), serving as the donor and acceptor of FRET, respectively. The FRET biosensor, endowed with NES, swiftly diffuses throughout the cytoplasm, leading to a compromised spatial resolution within individual cells with respect to ERK activation. The male hyBRET-ERK-NES mouse line was maintained in the heterozygous state. For the procurement of fetal mouse lung tissues, mating was carried out with female ICR mice purchased from Japan SLC (Slc:ICR). The trio breeding method was employed in our breeding program. In other instances, pregnant ICR mice procured from Japan SLC (Slc:ICR), were employed. We denoted the midnight preceding the detection of the vaginal plug as embryonic day 0.0 (E0.0), and pregnant mice underwent sacrifice via CO2 inhalation followed by cervical dislocation. Decapitation was employed for the euthanasia of embryonic mice. The mouse breeding and experimental protocols underwent scrutiny and received approval from the Institutional Animal Care and Use Committee at Kyoto University (approved numbers: MedKyo 18086, 19090, 20081, and 21043). The procedures strictly adhered to the guidelines governing the care and utilization of laboratory animals at Kyoto University. Daily monitoring revealed no instances of mortality, injuries, or clinical signs among the animals. Cages, shavings, and fresh enrichment materials were systematically replaced on a weekly basis.

METHOD DETAILS

Antibodies, small molecules, and recombinant proteins

The followings were used: rat monoclonal anti-E-cadherin (Cell Signaling Technology, #3195, 1:100 dilution), rabbit polyclonal anti-phospho-myosin light chain (pMLC) (Abcam, #ab2480, 1:100 dilution), Alexa Fluor 546-conjugated goat anti-rat IgG (H+L) antibody (Thermo Fisher Scientific, #A11081, 1:1000), Alexa Fluor 647-conjugated goat anti-rabbit IgG (H+L) antibody (Abcam, #ab150079, or Thermo Fisher Scientific, #A21247, 1:1000), Blebbistatin (Merck Millipore, #203391), CK-666 (Sigma-Aldrich, #SML0006), Cytochalasin D (Merck Millipore, #250255), Jasplakinolide (Abcam, #ab141409), Latrunculin A (Cayman Chemical, #10010630), Nocodazole (Merck Millipore, #487928), PD0325901 (FUJIFILM Wako Pure Chemical Corporation, #162-25291), SMIFH2 (Sigma-Aldrich, #S4826), Y-27632 (Merck Millipore, #SCM075), FGF1 (R&D Systems, #232-FA), and FGF7 (R&D Systems, #251-KG).

Ex vivo culture

Dissected lung lobes were placed onto a hydrophilic polytetrafluoroethylene organ culture insert with a pore size of 0.4 μm (Merck Millipore, #PICM01250), which was preset in a 35 mm petri dish filled with 800 μL of culture medium. Samples were cultured in an air-liquid interface at 37°C under 5% CO_2 conditions. To culture isolated epithelial tissues, dissected lobes were digested with 10 PU mL^{-1} of Dispase I (FUJIFILM Wako Pure Chemical Corporation, #386-02271) in phosphate buffered saline (PBS) for 15 min

on ice, and immersed into fetal bovine serum (FBS) and kept on ice for 5 min, to stop the protease-mediated reaction. Then, samples were washed in PBS twice on ice, and the distal tips of epithelial tissues were manually excised using fine needles. Isolated epithelial tissues were cultured within growth factor-reduced Matrigel (Corning, #356231) and covered with 500 μL of culture medium added to each well of glass bottom dishes (Greiner, #627870) at 37°C under 5% CO_2 conditions. We used FluoroBrite DMEM Media (Thermo Fischer Scientific, #A1896701) containing 1% GlutaMAX (Thermo Fischer Scientific, #35050061) and 0.5% FBS as the culture medium.

Whole-tissue immunofluorescence staining

Staining and optical clearing of dissected lung were performed according to previous studies.[63,64] Briefly, samples were fixed with 4% paraformaldehyde (PFA) in PBS overnight at 4°C. For pMLC staining, samples were fixed with 2% trichloroacetic acid in PBS containing a 1% phosphatase inhibitor cocktail (1:100, Nacalai Tesque, #07575-51) for 15 min at 4°C. Then, samples were blocked by incubation in 10% normal goat serum (Abcam, #ab156046) diluted in 0.1% Triton X-100/PBS (PBT) for 3 h at 37°C. Samples were treated with primary antibodies overnight at 4°C, washed in 0.1% PBT, and subsequently treated with secondary antibodies conjugated to either Alexa Fluor 546 or Alexa Fluor 647 overnight at 4°C. For nuclear counterstaining, we used Hoechst33342 (5 μg ml^{-1}, Dojindo Molecular Technologies, #H342) or DAPI (Dojindo Molecular Technologies, #D523-10, 1:200). The samples were mounted with 10 μL of 1% agarose gel onto a glass-based dish (Greiner Bio-One, #627871) for obtaining stable images. Then, samples were immersed with CUBIC-R+ (Tokyo Chemical Industry, #T3741) solution for 1 hour at 37°C or BABB solution (benzyl-alcohol and benzyl-benzoate, 1:2) for 30 min at 23°C.

F-actin and tubulin labeling

To visualize F-actin and microtubules, we used SiR-Actin and SiR-Tubulin, respectively,[65,66] according to the manufacturer's instructions (Cytoskeleton, #CY-SC001 and #CY-SC002). We added 1 μM of the far-red fluorogenic probes to the culture media, 1 hour before imaging. Although SiR-Actin was originally derived from Jasplakinolide, which activated ERK in isolated lung epithelial tissues in our experiments, ERK activation did not occur after treatment with SiR-Actin in isolated lung epithelial tissues.

Fluorescence labeling of FGF

To visualizes internalized FGFs, we used an amine-reactive pH-sensitive pHrodo iFL Red STP ester dye, according to the manufacturer's instructions (Thermo Fischer Scientific, #P36014). For the imaging of FGF1, regardless of its localization inside or outside cells, we used the Alexa Fluor 488 Microscale Protein Labeling Kit, according to the manufacturer's instructions (Thermo Fischer Scientific, #A30006).

Ethynyl deoxyuridine (EdU) assay

The lung epithelium was cultured within the Matrigel as described above for 3 hours with either 500 ng mL^{-1} FGF1 or 500 ng mL^{-1} FGF1 and 1 μM PD0325901 before the EdU incorporation to the lung epithelium. Next, 10 μM EdU dissolved into PBS was added to the culture media 20 min prior to the fixation with 4% PFA. Then, whole-tissue immunostaining of E-cadherin and nuclear counterstaining with DAPI were performed as described above. Then, EdU signal was detected using the Click-iT EdU Imaging Kits (Thermo Fisher Scientific, #C10340) according to the manufacture's instruction.

Microscopy

For live imaging, we used the incubator-integrated multiphoton fluorescence microscope system (LCV-MPE, Olympus) with a 25× water-immersion lens (NA=1.05, WD=2 mm, XLPLN25XWMP2, Olympus) or an inverted microscope (FV1200MPE-IX83, Olympus) with a 30× silicone-immersion lens (NA=1.05, WD=0.8 mm, UPLSAPO30XS, Olympus). The excitation wavelengths were set to 840 nm for the CFP of the ERK FRET biosensor, 930 nm for Alexa Fluor 488-labeled FGF1, and 1040 nm for the pHrodo iFL Red-labeled FGFs and the SiR probes (InSight DeepSee, Spectra-Physics). We used RDM690 IR cut filters (Olympus), and the DM505 and DM570 dichroic mirrors. We used BA460-500, BA495-540, BA520-560, BA575-630, and BA647/57 emission filters (Olympus) for CFP, Alexa Fluor 488, YFP or FRET, iFL Red probes, and SiR probes, respectively. For fixed samples, images were obtained using the Leica TCS SP8 confocal laser scanning platform equipped with the Leica HyD hybrid detector, using the 20× objective lens (NA=0.75, WD=680 μm, HC PL APO CS2, Leica) and 40× objective lens (NA = 1.3, WD = 240 μm, HC PL APO CS2, Leica).

Mechanical strain assay

We used a mechanical device (STREX, #STB-10) with a polydimethylsiloxane (PDMS) chamber (STREX, #STB-CH-04). To compress isolated epithelium, we placed isolated lung epithelial tissues in a 50% stretched state in the PDMS chamber, and added 1 mL of growth factor-reduced Matrigel (Corning, #356231), and performed gelation for 15 min at 37°C. Then, we added 2 mL of the culture medium supplemented with 500 ng mL^{-1} FGF1 into the chamber. We conducted experiments involving epithelial tissues under 2D culture conditions in the following manner. To obtain cell suspensions from primary tissues, lung tissues obtained via dissection at E12.5 were treated with 1 mg mL^{-1} Collagenase/Dispase (Sigma-Aldrich, #10269638001) in PBS for 50 min at 37°C while agitating the solution. Lung cells were then dispersed into the solution by gentle pipetting, and the suspended solution was filtered using a 40 μm pore size mesh (Corning, #352340). After centrifugation at 200G for 5 min at 25°C, the cell pellet was resuspended in a culture medium containing 10 μM Y-27632 and 10% KnockOut Serum Replacement (KSR) (Thermo Fischer Scientific, #10828010) and the

solution was placed in a PDMS chamber pretreated with a collagen coating (Cellmatrix Type I-C, Nitta Gelatin, #631-00771). After 2 days, the culture medium was exchanged with a medium not containing Y-27632 and KSR, 1 hour prior to imaging. Notably, the PDMS chamber gradually droops by becoming attached to the silicone oil used for objective lenses, because of which the focus has to be adjusted manually every time an image needs to be obtained. To quantify, we manually delineated the areas of epithelial cells to define the region of interest (ROI). Subsequently, we measured the FRET/CFP ratio, described above, in cytoplasmic regions within the ROI at pixel resolutions and calculated the average value in each sample. The values in Figure 3H are normalized to those obtained at the initial time point following the mechanical perturbation (1-2 min).

Osmolyte-based compression assay

The osmolyte-based tissue compression was performed according to the previous studies.[29,67] The lung epithelium was cultured within the Matrigel for 3 hours with 500 ng mL^{-1} FGF1 before the dextran administration. We used the dextran of 1500-2800 kDa in average molecular weight (Merck, #D5376) to prevent penetrating into the Matrigel. The culture medium was partially replaced into the dextran solution dissolved in the medium to reach the final concentrations for the compression. We converted the dextran concentration to the pressure based on the function of pressure versus dextran concentration[67]: 30 mg mL^{-1} for 2 kPa, and 55 mg mL^{-1} for 5 kPa. The time-lapse imaging was conducted at a single section along the z-axis. The distal region of lung epithelial tissues was manually defined as the area bounded by kink regions at the lateral sides of the distal tip to establish the ROI. To quantify ERK activity, we measured the FRET/CFP ratio in the cytoplasmic regions within the ROI at pixel resolutions, and the average value was calculated for each sample. The normalized ERK activity in Figure 3L was standardized to values obtained before the treatment with dextran. Tissue strain was evaluated by measuring the arclength of the basal side within the ROI before and after the dextran treatment.

Mathematical modeling and analysis

Apical length vs cell height at equilibrium

Here, we consider cells in a flat epithelial sheet to be identical, and assume that the basal edge length is almost the same as the apical edge length for the simplicity of analysis. Then, potential energy can be defined as follows:

$$U_{cell} = \frac{k_A}{2}(A - A^*)^2 + \frac{k_a}{2}(a - a^*)^2 + k_l l. \quad \text{(Equation 1)}$$

The first term represents the cell size constraint and its coefficient k_A, current cell area A, and the target cell area A^*. The second and third terms each represent the regulation of cell edge length at the apical and lateral side of cells a and l with controlling parameters k_a and k_l. We set the second term as a function that converges to the variable target apical length a^*, as explained later. Since the cell size was maintained even after a change in cell shape, caused by the inhibitor assay, we set $A = A^*$. Then, upon considering that $A = rh$, we can redefine Equation 1 as follows:

$$U^*_{cell} = \frac{k_a}{2}(a - a^*)^2 + k_l\frac{A^*}{a}, \quad \text{(Equation 2)}$$

Now, we have two variables, a and a^*, and obtained equilibrium values at the minimum potential energy value, i.e., $a_{eq} = (a|\partial U^*_{cell}/\partial a = 0)$ and $a^*_{eq} = (a^*|\partial U^*_{cell}/\partial a^* = 0)$ each, as $a_{eq} = \sqrt{A^* k_l/k_b}$ and $a^*_{eq} = a_{eq}$. From these equations, it was noted that $a^*_{eq} \sim l^{-1}_{eq}$, which indicates the existence of an inverse relationship between the apical length and cell height at equilibrium. The analysis in this section is based on that of a previous study.[68]

Apical length vs epithelial sheet curvature

The analysis in this section is based on that of a previous study.[69] Here, we considered the geometrical aspects of an epithelial monolayer, composed of smoothly-connected identical tetragons along a line. The curvature κ at the midplane of the epithelial sheet is represented as

$$\kappa = \frac{2}{a+b}\left(\pi - 2\cos^{-1}\frac{b-a}{2l}\right), \quad \text{(Equation 3)}$$

where a, b, and l denote the apical, basal, and lateral edge lengths, respectively. Then, the curvature with respect to the apical edge length is determined as follows:

$$\frac{\partial \kappa}{\partial a} = -\frac{2}{l(a+b)\sqrt{1-\{(a-b)/4l\}^2}} - \frac{2}{(a+b)^2}\left(\pi - 2\cos^{-1}\frac{b-a}{2l}\right) < 0 \quad \text{(Equation 4)}$$

This indicates that the sheet curvature becomes small with an increase in the apical edge length.

Mathematical modeling for multicellular dynamics

We modeled an epithelial monolayer using the vertex model framework.[34–36] In our model, a single cell is represented as a polygon with four vertices and edges, which are shared by neighboring cells. The dynamics of vertex position $\mathbf{r}_i$, where i is an index of the vertex, obeys the equation of motion, based on the principle of least potential energy U, with a drag coefficient η and luminal pressure p as follows:

$$\eta\dot{\mathbf{r}}_i = -\nabla_i U + f(p) \quad \text{(Equation 5)}$$

To determine the potential energy in the first term, we defined a minimal expression:

$$U = \sum_j \left\{ \frac{k_A}{2}\left(A_j - A_j^*\right)^2 + \frac{k_a}{2}\left(a_j - a_j^*\right)^2 + k_l l_j \right\} + \sum_i \frac{k_\theta}{2}\left\{ (\theta_{i_+} - \pi/2)^2 + (\theta_{i_-} - \pi/2)^2 \right\}. \quad \text{(Equation 6)}$$

The first term represents the cell size constraint with its coefficient k_A, current cell area A_j, and the target cell area A_j^*. The second and third terms each represent the regulation of the cell edge length at the apical and the lateral sides of cells a_j and l_j, with controlling parameters k_a and k_l. As the apical edge is controlled by the ERK activation level, we set the second term as a function that converges to the variable target apical length a_j^*; this has been explained later. The fourth and fifth terms represent the bending energy of cells at the apical and the basal sides, attributed to each vertex i; k_θ denotes the bending rigidity, and θ_{i_+} and θ_{i_-} are angles at the vertex i across the cell edge.

The second term of Equation 5 represents the mechanical effect of luminal pressure[38,39,55] on the apical edge of epithelial cells. The function f was defined as

$$f(p) = p\mathbf{n}_i, \quad \text{(Equation 7)}$$

where p is strength of pressure, and $\mathbf{n}_i$ is the normal vector at the apical vertex i. Note that this function is effective only at vertices in the apical sides of cells.

To implement cell proliferation, we ensured that each cell was set with the cell timer τ_j, and all cells had the same cell cycle length τ_{div}. We assumed that cell cycle progression depended on the ERK activity, namely the curvature in the model; i.e., the cell cycle progresses when the cell curvature is not less than zero ($\kappa_j \geq 0$), and the cell cycle pauses when the cell curvature is less than zero ($\kappa_j < 0$), according to the previous report[40] and cell proliferation assay (Figure S6). This is also attributable to the fact that cell proliferation in the developing murine lung requires ERK activation, which can be observed in the distal tip.[18,22] Cell division occurs and cells with almost equal sizes are produced when the cell timer reaches the cell cycle length, $\tau_j = \tau_{div}$. Once cell division occurs, the τ_j value in one of the daughter cells resets to zero and that in another is set at a value chosen stochastically from 0 to $0.05\tau_{div}$ with a uniform distribution, to avoid perfect synchronization between neighboring cells.

In our model, the target apical edge length depends on the cytoskeletal level c, observed with a level of F-actin accumulation, as follows:

$$a_j^* = \zeta g(c_j) + a_0 \quad \text{(Equation 8)}$$

$$g(c_j) = \begin{cases} -1, & c_j \leq -1 \\ c_j, & -1 < c_j < 1 \\ 1, & 1 \leq c_j \end{cases} \quad \text{(Equation 9)}$$

Here, ζ denotes the maximum length after edge extension, and a_0 is the baseline for the apical edge length. The saturation function g represents the physical limit for the change in edge length. We modeled the cytoskeletal level c as follows:

$$\dot{c_j} = \alpha \tanh(\lambda \kappa_j) H(\kappa_j) + \beta - \gamma c_j. \quad \text{(Equation 10)}$$

The first term $\dot{c_j}$ represents the curvature-dependent contribution of FGF-ERK, along with the magnitude parameter α and the sensitivity parameter λ, to the curvature κ. H is the step function of the curvature, i.e., H=1 for $\kappa \geq 0$ and H=0 for $\kappa < 0$. The curvature κ_j at cell j is calculated using the spline function-based method described above. As the cytoskeleton level controls the apical target length observed with an increase in the monotonic function, as shown in Equation 9, curvature-dependent apical extension/shrinkage is represented as a positive/negative α value. The second term represents the curvature-independent contribution of FGF-ERK, along with the parameter β. The third term represents the decay of cytoskeletons, including F-actin depolymerization and severing. The rate γ controls the characteristic decay time; the inverse value ofγ denotes the retention time for cell curvature memory. The level of curvature-dependent FGF-ERK activation was determined in Equation 10 because of its rapid response.

Numerical simulations

We considered a manually traced line along the basal sides of cells in the image shown in Figure 1 as the initial shape for the simulation, when the diameter of the distal tip D was in the measured range. Upon an analysis of the tissue morphology, the number of cells was determined according to the measured cell size, i.e., the average cell width and cell height, which were 5 μm and 20 μm, respectively. The boundary in the proximal side was fixed in the simulations shown in Figures 6B and 6C. For the simulations in Figures 6D–6I, we used the symmetrical image created based on the Figure 6A. Ordinary differential equations were numerically solved using the forward Euler method, with a time step of 0.01, using MATLAB (MathWorks). The simulations were terminated when the number of cells was more than 300.

Standard parameters were set as follows: $\eta = 1$, $k_A = 0.01$, $k_a = 1$, $k_l = 0.2$, $k_\theta = 20$, $\tau_{div} = 300$, $\alpha = 1$, $\beta = 0$, $\gamma = 0.001$, $\zeta = 3\ \mu m$, $\lambda = 100$, $p = 0.05$, and $D = 70\ \mu m$, unless otherwise noted. Thek_A, k_a, k_l, k_θ, λ, and p values were determined by numerical analyses using several criteria, under which the simulated curvature imitates the experimental observations and became insensitive to the change in the values, as shown in Figure S5. The maximum length of edge extension, i.e., the ζ value, was determined from our measurements. A_j^* and a_0 values were set according to the initial conditions, e.g., $A_j^* = 93\ \mu m$ and $a_0 = 4\ \mu m$ when $D = 70\ \mu m$.

QUANTIFICATION AND STATISTICAL ANALYSIS

FRET image analysis

The median filter of a 3 × 3 window was processed to remove shot noise, and the background signal was subtracted from each FRET and CFP channel. Then, the ratio of FRET intensity to CFP intensity was calculated using a custom-made MATLAB (MathWorks) script. In the scale bar, the color represents the FRET/CFP ratio and brightness represents the fluorescence intensity of the FRET channel.

Three-dimensional mapping

To determine the correlation between different quantities, such as ERK activity, F-actin signal, tissue curvature, and tissue thickness (Figure S1A), we obtained 3D stacked images of lung epithelial tissues with 1-μm-long z-intervals, and manually traced either the basal or apical side of the cells. Next, we generated triangle meshes on the traced surface using "Iso2Mesh," a free mesh generation toolbox.[70] Then, we calculated a discrete Gaussian curvature and a discrete curvature on each node of generated meshes using a custom-made code according to the definition proposed earlier.[71] Finally, we obtained all values except those for the curvatures by averaging values around the nodes, and mapped them at each node. All processing was performed using MATLAB.

Curvature measurement in 2D

We used a spline curve-based method described elsewhere.[58] Briefly, we manually traced the basal side of epithelial cells from images, and determined discrete sampling points (x_i, y_i) along traced curves at regular intervals. Upon fitting the 4 sampling points from i-1 to i+2 with a cubic spline function, the function S_i at an interval $[x_i, x_{i+1}]$ was denoted as $S_i(x) = a_i(x - x_i)^3 + b_i(x - x_i)^2 + c_i(x - x_i) + d_i$. Due to the definition of the curvature using the formula $\kappa(x) = S''(1+S'^2)^{-3/2}$, the curvature from the spline function was calculated as follows:

$$\kappa_i(x) = \frac{6a(x - x_i)+2b}{\left(1+\left\{3a(x - x_i)^2+2b(x - x_i)+c\right\}^2\right)^{3/2}}.$$

The convex/concave surface of the lumen was assigned a positive/negative value, namely κ. We defined tissue thickness as the length from the apical to the basal edge, which is vertical to the traced curve at the sampling points.

Statistical hypothesis testing

The number of cells or regions of interest analyzed (n) and the number of biological replicates (N) are indicated in the figure legends. No particular statistical method was used to predetermine the sample size. A minimum of N=3 independent experiments were performed, based on previous studies in the field. No inclusion/exclusion criteria were used and all analyzed samples were included in the analysis. No randomization was performed. Statistical tests, sample sizes, test statistics, and *P*-values have been described in the main text. We considered P-values < 0.05 to be statistically significant in two-tailed tests, and classified them into the following 4 categories: * ($p<0.05$), ** ($p<0.01$), *** ($p<0.001$), and n.s. (not significant, i.e., $p \geq 0.05$).

Graph

In the boxplot, the central mark indicates the median, and the bottom and top edges of the box indicate the 25th and 75th percentiles, respectively. The whiskers extend to the most extreme data points not considered to be outliers, and the outliers are plotted individually using the '+' symbol. All the graphs were drawn using MATLAB.